Numerical Computations for Ion Probe Characteristics in a Collisionless Plasma

by

Francis F. Chen

MATT-252 February, 1964

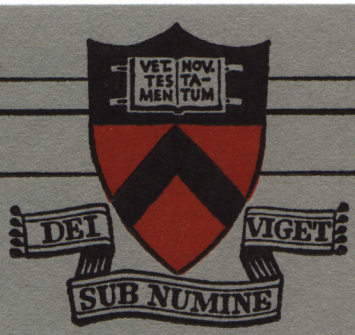

PLASMA PHYSICS LABORATORY

Contract AT(30-1)—1238 with the
US Atomic Energy Commission

PRINCETON UNIVERSITY
PRINCETON, NEW JERSEY

Princeton University
Plasma Physics Laboratory
Princeton, New Jersey

Numerical Computations for Ion Probe Characteristics in a Collisionless Plasma

by

Francis F. Chen

MATT-252 February, 1964

AEC RESEARCH AND DEVELOPMENT REPORT

This work was supported under Contract AT(30-1)-1238 with the Atomic Energy Commission.

Numerical Computations for Ion Probe Characteristics in a Collisionless Plasma

Francis F. Chen

ABSTRACT

Numerical results in ranges of experimental interest are presented in graphical form for the potential profile around negatively biased spherical and cylindrical probes in a collisionless plasma and for the saturation ion current-voltage characteristics. The computations were made on the basis of the theories of Allen, Boyd, and Reynolds for zero ion temperature and of Bernstein and Rabinowitz for monoenergetic ions. These theories are useful primarily for small probes. For large probes the theory of Lam is applicable. For completeness we have also included whatever curves are necessary for the use of Lam's theory.

1. INTRODUCTION

The recent boundary-layer analysis of Lam[1] puts the theory of electrostatic probes in a collisionless plasma into definitive form. As long as collisions and magnetic fields do not play a role, and as long as the experimental difficulties of particle trapping and of reflection, secondary emission, changes of work function, and so forth at the probe surface can be overcome, the current to a biased probe can now be predicted rigorously by theory. However, in some situations tedious numerical computation is necessary. It is the purpose of this report to assemble under a single cover such numerical results as may be needed by an experimentalist, in a form which is convenient to use.

The situation may be summarized as follows. For collection of the hotter species, usually electrons, the original theory of Langmuir[2] is valid. For collection of the colder species, usually ions, Langmuir's orbital theory may still be used if $a \ll h$ (symbols are defined in Sec. 2). The case $a \gg h$ is covered by the theory of Lam.[1] In the limit of large a or small η_p this theory reduces to the well-known result of Bohm, Burhop, and Massey[3] and of Wenzl.[4] Lam's theory is more rigorous and more convenient to use than the earlier theory by Wenzl.[4] The case $a \approx h$ is covered by the theory of Allen, Boyd, and Reynolds[5] (ABR) for $\beta = 0$ and by the theory of Bernstein and Rabinowitz[6] (BR) for $0 < \beta < 1$. This case is the troublesome one and necessitates the numerical computations whose results are presented in this report.

We have concentrated attention on the simpler equations of ABR,[5] which give a fairly good approximation for $\beta < 0.1$, especially in the spherical case. In addition to the probe characteristics we have given the potential distributions so that the reader may make his own cross-plots if that is necessary. The computations were made on an IBM 7090 and cover a wider range of parameters than given by ABR.[5] In the case of the BR theory, we have extended the original computations only in the cylindrical case. However, we wish to point out that because of a number of misprints the original paper of BR gives incorrect numerical results and should be used only for the formulation of the theory.

The curves contained herein replace the need to approximate by "patching" the Bohm[3] current to the $V^{3/2}$ space-charge law. This procedure, used previously by Kagan and Perel,[7] Schulz and Brown,[8] Boyd and Thompson,[9] and Ichimiya, Takayama, and Aono,[10] is both more laborious and less accurate.

The proper theory to use for saturation ion currents is shown in Table I for various ranges of parameters. The probe voltage η_p enters because it affects the distribution of the electrons. For $\eta_p \gg 1$, the electron distribution may be considered Maxwellian. For η_p less than about 1/2 or 1, the quasi-neutral solution holds everywhere, and probe theory is particularly simple. For $1 < \eta_p < 5$, the deviation from a Maxwellian distribution due to the loss of electrons to the probe must be taken into account. Although this poses no problem in principle, it complicates the computations. It is understood that the above remarks apply equally well to electron collection when

the ions are nearly Maxwellian; however, for saturation electron currents the need for Table I does not arise unless $T_e < T_i$. The case $1 < \eta < 5$ is, of course, interesting for the computation of the floating potential.

Although our computations have been made only for monoenergetic ions, it is clear that the results for a Maxwellian distribution will not be appreciably different for $\beta << 1$, since the dependence on ion energy is slight. On the other hand, for $\beta >> 1$ the probe current depends primarily on kT_i and is given by Langmuir's sheath theory for a Maxwellian distribution. The transition case $\beta \approx 1$ is not well covered by any simple theory. The simple sheath theory fails because the accelerating electric field outside the sheath is neglected; the BR theory fails because a monoenergetic distribution is no longer a good approximation. This gap in the theory has been plugged recently by Hall,[11] who has found a method to integrate numerically the BR equations for a Maxwellian distribution.

Finally, we wish to point out that whenever possible spherical probes should be used in preference to cylindrical probes for the following reasons:

(1) The disturbance of the plasma by the probe is smaller for a sphere because the potential falls off faster with radius.

(2) For a given radius, a cylindrical probe is more likely to trap ions in closed orbits; that is, it must be operated at lower potential than a spherical probe. Conversely, for a given η_p a cylindrical probe must be made larger in diameter in order to avoid ion trapping.

(3) Spherical probes are not sensitive to the distribution of angular momenta assumed at infinitity..

(4) For spherical probes the theory is simpler, and numerical computations are easier to carry out.

These remarks are of course not applicable in the presence of a strong magnetic field.

2. DEFINITIONS

C. g. s. - e. s. u. are used. All currents are particle currents multiplied by the charge number of the particle. The subscript p indicates probe surface; the subscript o indicates absorption radius; and the subscript 1 indicates the radius where the quasi-neutral solution breaks down.

$\eta = -eV/kT_e$ (normalized potential)

$\xi = r/h$ (normalized radius)

$\xi_p = r_p/h$ or a/h (normalized probe radius)

$h = (kT_e/4\pi n_o e^2)^{\frac{1}{2}}$ (Debye length)

n_o = plasma density at ∞

E_i = ion energy at ∞, for a monoenergetic distribution

$\beta = E_i/ZkT_e$ (normalized ion energy)

Z = charge number of the ions

$J = I_i (e^2/kT_e)(m_i/2Z\,kT_e)^{\frac{1}{2}}$ (normalized ion current for spheres)

$J = I_i (e/kT_e)(m_i/2\pi n_o Z)^{\frac{1}{2}}$ (normalized ion current for cylinders)

I_i = total ion current to probe for spheres

I_i = ion current per unit length to probe for cylinders

$J\xi_p = I_i r_p (e/kT_e)^2 (2m_i kT_e/Z)^{\frac{1}{2}}$ (another useful normalization for cylinders)

$\zeta = \xi J^{-\frac{1}{2}}$ (another useful normalization for spheres)

$\zeta = \xi J^{-1}$ (another useful normalization for cylinders)

L = angular momentum

ℓ = mean free path of ions

$\iota = I_i (m_i/2ZkT_e)^{\frac{1}{2}}/(\pi r_p^2 n_o)$ (normalized ion current in Lam's theory, for spheres)

$\iota = I_i (m_i/2ZkT_e)^{\frac{1}{2}}/2r_p n_o)$ (normalized ion current in Lam's theory, for cylinders)

ι_B = normalized Bohm current, a function of β only

$I_B = \pi r_p^2 n_o \iota_B (2ZkT_e/m_i)^{\frac{1}{2}}$ (Bohm current to sphere, valid for $\xi_p \to \infty$)

$I_B = 2r_p n_o \iota_B (2ZkT_e/m_i)^{\frac{1}{2}}$ (Bohm current to cylinder, valid for $\xi_p \to \infty$)

$I_{eo} = n_o (kT_e/2\pi m_e)^{\frac{1}{2}}$

$\tau = \iota/\iota_B = I_i/I_B$ (a ratio expressing the increase in ion current over the Bohm value, due to finite sheath thickness)

$\Lambda_s(\tau)$, $F(T)$ = functions used in Lam's theory for spheres

$\Lambda_c(\tau)$, $G(\psi)$ = functions used in Lam's theory for cylinders

3. FORMULAS AND GRAPHS

For $\beta = 0$ we have used the following equation[5] for a spherical probe:

$$\frac{d}{d\xi}\left(\xi^2 \frac{d\eta}{d\xi}\right) - J\eta^{-\frac{1}{2}} + \xi^2 e^{-\eta} = 0 \ . \qquad (1)$$

The results for the potential distribution $\eta(\xi)$ for various values of J are shown in Fig. 1, where for convenience of presentation we have plotted η vs. the variable $\zeta = \xi J^{-\frac{1}{2}}$. In terms of ζ, Eq. (1) can be written

$$\frac{1}{J}\frac{d}{d\zeta}\left(\zeta^2 \frac{d\eta}{d\zeta}\right) - \eta^{-\frac{1}{2}} + \zeta^2 e^{-\eta} = 0 \ , \qquad (2)$$

so that the quasi-neutral solution is the same for all J. A log-log plot of $\eta(\xi)$ is given in Fig. 2 for easier reading at the extremes of the range of ξ. The log ξ - log J cross-plot of Fig. 3 is used for interpolating in J to obtain the probe characteristics $J(\eta_p)$. The latter are shown for various ξ_p on a linear scale in Figs 4a and 4b, and on a logarithmic scale in Fig. 5. From Fig. 5 one can see the range in which J varies as $\eta_p^{\frac{1}{2}}$. To find the plasma density, one computes J from the experimental data, using a known value of kT_e, and places the points on Fig. 4. The value of ξ_p is then obtained, from which n_o can be computed. From the curves $\eta(\xi)$ the reader may make whatever cross-plots he wishes if the ones presented here are not convenient.

For $\beta = 0$ we have used the following equation for a cylindrical probe:

$$\frac{d}{d\xi}\left(\xi \frac{d\eta}{d\xi}\right) - J\eta^{-\frac{1}{2}} + \xi e^{-\eta} = 0 \ . \qquad (3)$$

In terms of $\zeta = \xi J^{-1}$, this reads

$$\frac{1}{J^2}\frac{d}{d\zeta}\left(\zeta\frac{d\eta}{d\zeta}\right) - \eta^{-\frac{1}{2}} + \zeta e^{-\eta} = 0 \ . \tag{4}$$

These equations are valid if the distribution of angular momenta L at ∞ is a delta function around L = 0. In practice the collisionless equations are valid only up to a mean free path $\underline{\ell}$, and the validity condition can be written:

$$\frac{-E_i}{eV_p} \ll \frac{r_p^2}{\ell^2} \ . \tag{5}$$

The potential distribution $\eta(\zeta)$ is shown in Fig. 6. A log-log plot of $\eta(\xi)$ is given in Fig. 7. The log ξ-log $J\xi$ cross-plot is given in Fig. 8. From this one obtains the probe characteristics $J\xi_p(\eta_p)$ for various ξ_p shown linearly in Figs. 9a, 9b, and 9c, and logarithmically in Fig. 10. From the latter one can see the range in which $J\xi_p$ varies as $\eta_p^{\frac{1}{2}}$. The quantity $J\xi_p$ is used because it is independent of n_o. To find the plasma density when kT_e is known, one computes $J\xi_p$ from the experimental data and places the points on Fig. 9. A value of ξ_p is then obtained, from which n_o is easily calculated.

For finite β we have used the following equation[6] for a <u>spherical probe</u>:

$$\frac{1}{\xi^2}\frac{d}{d\xi}\left(\xi^2\frac{d\eta}{d\xi}\right) = \tfrac{1}{2}\left(1+\frac{\eta}{\beta}\right)^{\frac{1}{2}} \pm \tfrac{1}{2}\left[1+\frac{\eta}{\beta}-\frac{4J}{\beta^{\frac{1}{2}}\xi^2}\right]^{\frac{1}{2}} - e^{-\eta} \ , \tag{6}$$

where the plus sign is used for the exterior region $\xi \geq \xi_o$ and the minus sign for the interior region $\xi \leq \xi_o$. The absorption radius ξ_o occurs when the square bracket vanishes.

The potential profiles $\eta(\xi)$ for various J have been taken from the computations of Bernstein and Rabinowitz[6] and are shown in Fig. 11a, 11b, and 11c for $\beta = 0.01$, 0.05, and 0.1, respectively. The cross-plots $J(\eta_p)$ for various ξ_p are shown in Fig. 12a, 12b, and 12c. These are the probe characteristics. To show the dependence on β, we have plotted in Fig. 13 the probe characteristics for $\xi_p = 10$ and various values of β, including $\beta = 0$ from Fig. 4. In general, the dependence on β is small for large ξ_p and becomes measurable for $\xi_p \lesssim 10$. A log-log plot of $J(\eta_p)$ for various ξ_p is given in Fig. 14 for $\beta = 0.1$ to show the range in which J varies approximately as $\eta_p^{\frac{1}{2}}$. The plasma density is found the same way as in the $\beta = 0$ case, only an approximate value of β must now be chosen. These results are valid for a monoenergetic, isotropic ion distribution but because of the insensitivity to β for $\beta \ll 1$ they may be applied to a Maxwellian distribution of such a temperature that the random current is kept the same; thus the equivalent ion temperature is

$$\begin{aligned} &\text{Spheres:} && kT_i = \frac{\pi}{4} E_i = \frac{\pi}{4} \beta Z k T_e \,. \\ &\text{Cylinders:} && kT_i = \frac{4}{\pi} E_i = \frac{4}{\pi} \beta Z k T_e \,. \end{aligned} \tag{7}$$

For finite β we have used the following equation[6] for a cylindrical probe:

$$\frac{1}{\xi} \frac{d}{d\xi} \left(\xi \frac{d\eta}{d\xi} \right) = \left\{ \begin{matrix} 1 \\ 0 \end{matrix} \right\} - \frac{1}{\pi} \sin^{-1} \left[\frac{\pi J}{\xi (\beta + \eta)^{\frac{1}{2}}} \right] - e^{-\eta} \,, \tag{8}$$

where the top choice is for $\xi \geq \xi_o$ and the bottom choice is for $\xi \leq \xi_o$. The absorption radius ξ_o occurs when the square bracket is unity. The data of Bernstein and Rabinowitz[6] for the potential profiles $\eta(\xi)$ for various

β and J are plotted in Fig. 15a,b,c,d,e, and f to show the shape of $\eta(\xi)$ and the dependence on β. New computations for $\eta(\xi)$ at various J for $\beta = 0.01$, 0.03, and 0.1 are shown in Fig. 16a,b, and c on log-log plots. The behavior of a typical quasi-neutral curve is also shown. From Fig. 16c one obtains by cross plotting the probe characteristics $J\xi_p(\eta_p)$ for various values of ξ_p. These are shown in Fig. 17 for $\beta = 0.1$; the β-dependence is so small that we have not bothered to plot other values of β. We have plotted $J\xi_p$ rather than J because $J\xi_p$ is independent of n_o; the density can then be determined as in the $\beta = 0$ case. Unfortunately, large values of ξ_p for large η_p could not be obtained with the program used. In Fig. 18 we show the probe characteristics on a log-log scale to make clear the range in which J varies approximately as $\eta_p^{\frac{1}{2}}$.

Equation (8) is based on the assumption of a distribution of angular momenta L at ∞ which is independent of L. Hence the assumed distribution is not isotropic in the cylindrical case; it is monoenergetic in $E_{i\perp}$ and arbitrary in $E_{i\parallel}$; the projections of the velocities on a plane perpendicular to the probe axis are isotropic. However, because of the insensitivity to β, the present results may also be used for a Maxwellian distribution if $\beta \ll 1$. If one takes the limit of Eq. (8) as $\beta \to 0$, one does not recover Eq. (3) for $\beta = 0$ unless the arc sin may be replaced by its argument. The reason for this lies in the indeterminacy of L as $\xi \to \infty$. When the inequality (5) is not satisfied, Eq. (8) should be used. This problem does not arise for the sphere. We have not computed the $\beta = 0$ case with Eq. (8); however, for large ξ_p and η_p the difference between Eqs. (3) and (8) should be small.

For large ξ_p the probe characteristics are more easily computed by the method of Lam.[1] For this one uses the Lam diagram of Fig. 19. Suppose r_p, n_o, kT_e, and β are known; then the β-dependent coefficient A of Fig. 19 is found from Fig. 20 for spheres and Fig. 21 for cylinders and $A\xi_p^{-4/3}$ is computed. For a given η_p, one follows a path like the dotted one shown in the upper half of Fig. 19 to find I_i/I_B, where I_B is the Bohm current defined in Sec. 2. The electron component can be found similarly from the lower half of Fig. 19. Strictly speaking, the curves of constant I_{eo}/I_B for each element depend on β; but we have neglected this slight variation. The coefficient A is defined by

$$A = (4/\iota_B)^{2/3} \quad \text{(spheres)}$$

$$A = (\pi/\iota_B)^{2/3} \quad \text{(cylinders)} \ , \tag{9}$$

where ι_B is found from the following transcendental equations:

Spheres:
$$\iota_B = 4\, e^{-\eta_1} \left[\tfrac{1}{2}(\eta_1 + \beta)^{-\frac{1}{2}} + \beta^{\frac{1}{2}}\, e^{-\eta_1}\right] \tag{10}$$

$$\eta_1 = \tfrac{1}{2} - \beta + 2\beta^{\frac{1}{2}} (\eta_1 + \beta)^{\frac{1}{2}}\, e^{-\eta_1} \tag{11}$$

Cylinders:
$$\iota_B = (\eta_1 + \beta)\, \sin(\pi\, e^{-\eta_1}) \tag{12}$$

$$\tan(\pi\, e^{-\eta_1}) = 2(\eta_1 + \beta)\, \pi\, e^{-\eta_1} \ . \tag{13}$$

Values of ι_B and η_1 obtained by hand computation and graphical methods are shown in Figs. 20 and 21.

To determine the plasma density one uses the following formulas (in e.s.u.):

$$\text{Sphere:} \qquad \frac{-V_p}{(e I_i)^{2/3}} = \left(\frac{m_i}{2Ze}\right)^{\frac{1}{3}} \Lambda_s(\tau) \tag{14}$$

$$\text{Cylinder:} \qquad \frac{-V_p}{(e I_i a)^{2/3}} = \left(\frac{2m_i}{Ze}\right)^{\frac{1}{3}} \Lambda_c(\tau) \ , \tag{15}$$

where

$$\tau = \iota/\iota_B = I_i/I_B \ . \tag{16}$$

The l.h.s. is computed from the experimental data; then, having $\Lambda_s(\tau)$ or $\Lambda_c(\tau)$, one finds τ from Figs. 22, 23, or 24. Knowing τ, one finds I_i from ι_B given in Figs. 20 or 21. The function $\Lambda_s(\tau)$ is defined as

$$\Lambda_s(\tau) = F(\tau^{\frac{1}{2}}) \ , \tag{17}$$

where F is the solution of the equation

$$T^2 F^{\frac{1}{2}} \, d^2F/dT^2 = 1 \tag{18}$$

subject to the boundary conditions $F = F' = 0$ at $T = 1$. The function $\Lambda_c(\tau)$ is defined as

$$\Lambda_c(\tau) = \tau^{2/3} \, G(\tau) \ , \tag{19}$$

where G is the solution of the equation

$$\psi^2 G^{\frac{1}{2}} \frac{d}{d\psi}\left(\psi \frac{dG}{d\psi}\right) = 1 \tag{20}$$

under the same boundary conditions. The curves in the Lam diagram (Fig. 19) are of the functions $\tau^{2/3}\Lambda_s(\tau)$ and $\tau^{2/3}G(\tau)$. The dashed portions of the curves in Figs. 19, 22, and 23 indicate the region where trapped ions are possible.

Since very often ion trapping does not occur even when it can, it is possible to use much higher voltages or smaller probes than the trapping criterion dictates. The functions $\Lambda_s(\tau)$ and $\Lambda_c(\tau)$ for this extended range of τ, where trapping can occur, are shown in Fig. 24. The curves $\tau^{2/3}\Lambda_s(\tau)$ and $\tau^{2/3}\Lambda_c(\tau)$, which are the ones in the first quadrant of the Lam diagram (Fig. 19) are shown for this extended range in Fig. 25.

In Fig. 26 we show τ^2 vs. $A\xi_p^{-4/3}\eta_p$ in the "normal" range of τ. This is essentially an $I_i^2 - V_p$ plot and shows that such a plot can be approximated by a straight line. In Fig. 27 we show the same plot for the extended range of τ.

All of the results in this report are subject to the restriction $\eta_p \gtrsim 4$ so that the electron distribution is approximately Maxwellian.

4. ACKNOWLEDGMENTS

The author is indebted to Mrs. J. Peskin for performing the calculations for finite β on an IBM 704 computer, to Mr. H. Fishman for the calculation for $\beta = 0$ on an IBM 7090, and to Mr. K. P. Mann for plotting and tracing the numerous curves.

REFERENCES

1. S. H. Lam, Phys. Fluids 7 (1964).

2. I. Langmuir, Collected Works, G. Suits, ed. (Pergamon Press, New York, 1961), Vol. 4, p. 99.

3. D. Bohm, E. H. S. Burhop, and H. S. W. Massey, in The Characteristics of Electrical Discharges in Magnetic Fields, ed. by A. Guthrie and R. K. Wakerling (McGraw-Hill Book Co., New York, 1949), Chap. 2.

4. F. Wenzl, Z. angew, Phys. 2, 59 (1950).

5. J. E. Allen, R. L. F. Boyd, and P. Reynolds, Proc. Phys. Soc. 70B, 297 (1957).

6. I. B. Bernstein and I. Rabinowitz, Phys. Fluids 2, 112 (1959).

7. Yu. M. Kagan and V. I. Perel, Doklady Akad. Nauk SSSR 91, 1321 (1953).

8. G. J. Schulz and S. C. Brown, Phys. Rev. 98, 1642 (1955).

9. R. L. F. Boyd and J. B. Thompson, Proc. Roy. Soc. 252A, 102 (1959).

10. T. Ichimiya, K. Takayama, and Y. Aono, in Space Research: Proc. 1st Int'l Space Science Symposium, Nice, 1960 (North Holland Publ. Co., Amsterdam, 1960), p. 397.

11. L. S. Hall, Report UCRL-7660-T (1964).

TABLE I

Ion Distribution	β	Geom.	$a \ll h$	$a \approx h$			$a \gg h$		
			all η_p	$\eta_p \gg 1$	$1<\eta_p<5$	$\eta_p < 1$	$\eta_p \gg 1$	$1<\eta_p<5$	$\eta_p<1$
—	0	Sph.		ABR*			Lam* (ABR)		Lam
		Cyl.		C*			C*		
Mono-energetic	$<<1$	Sph.	L-0	BR*			Lam* (B,W)	Lam†	Lam
		Cyl.	L-0	BR*		L-0	Lam* (W)	Lam†	Lam
	≈ 1	Sph.	L-0	BR			Lam* (B,W)	Lam†	Lam
		Cyl.	L-0	BR		L-0	Lam* (W)	Lam†	Lam
	$>>1$	Sph.	L-0	BR		L-0	L-S		L-0
		Cyl.	L-0	BR		L-0	L-S		L-0
Maxw.	$<<1$	Sph.	L-0	BR†			BR†		
		Cyl.	L-0	BR†		L-0	BR†		
	≈ 1	Sph.	L-0	H (BR†)			H (BR†)		
		Cyl.	L-0	H (BR†)			H (BR†)		
	$>>1$	Sph.	L-0	BR†		L-0	L-S		L-0
		Cyl.	L-0	BR†		L-0	L-S		L-0

TABLE I - LEGEND

*	Numerical computations available in this report
/	Formalism indicated only
( )	Superseded work
L-0	Langmuir orbital-motion theory (Ref. 2)
L-S	Langmuir sheath theory (Ref. 2)
ABR	Allen, Boyd, and Reynolds (Ref. 5)
BR	Bernstein and Rabinowitz (Ref. 6)
Lam	Lam (Ref. 1)
B	Bohm, Burhop, and Massey (Ref. 3)
W	Wenzl (Ref. 4)
H	Hall (Ref. 11)
C	Chen (present report)

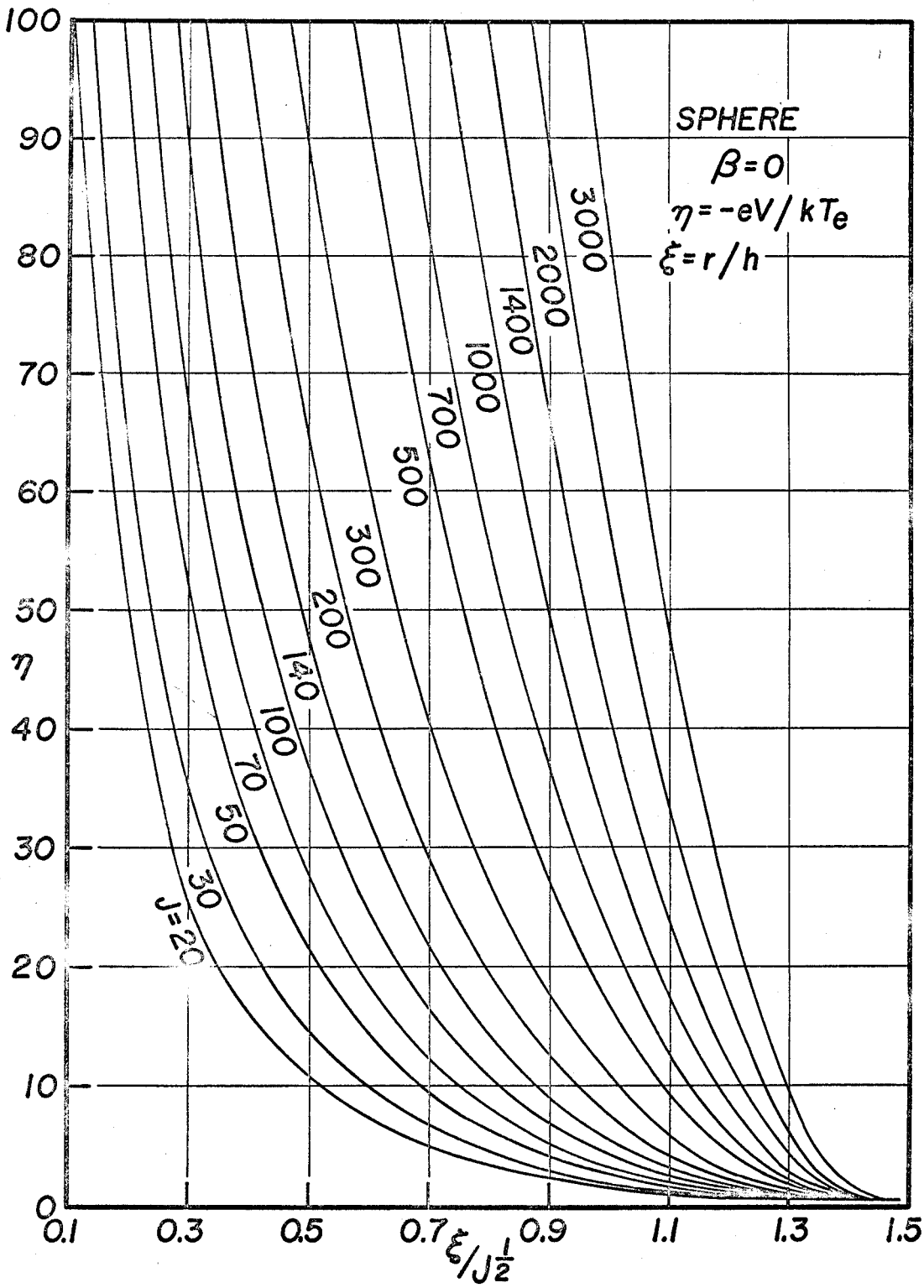

Figure 1

643124

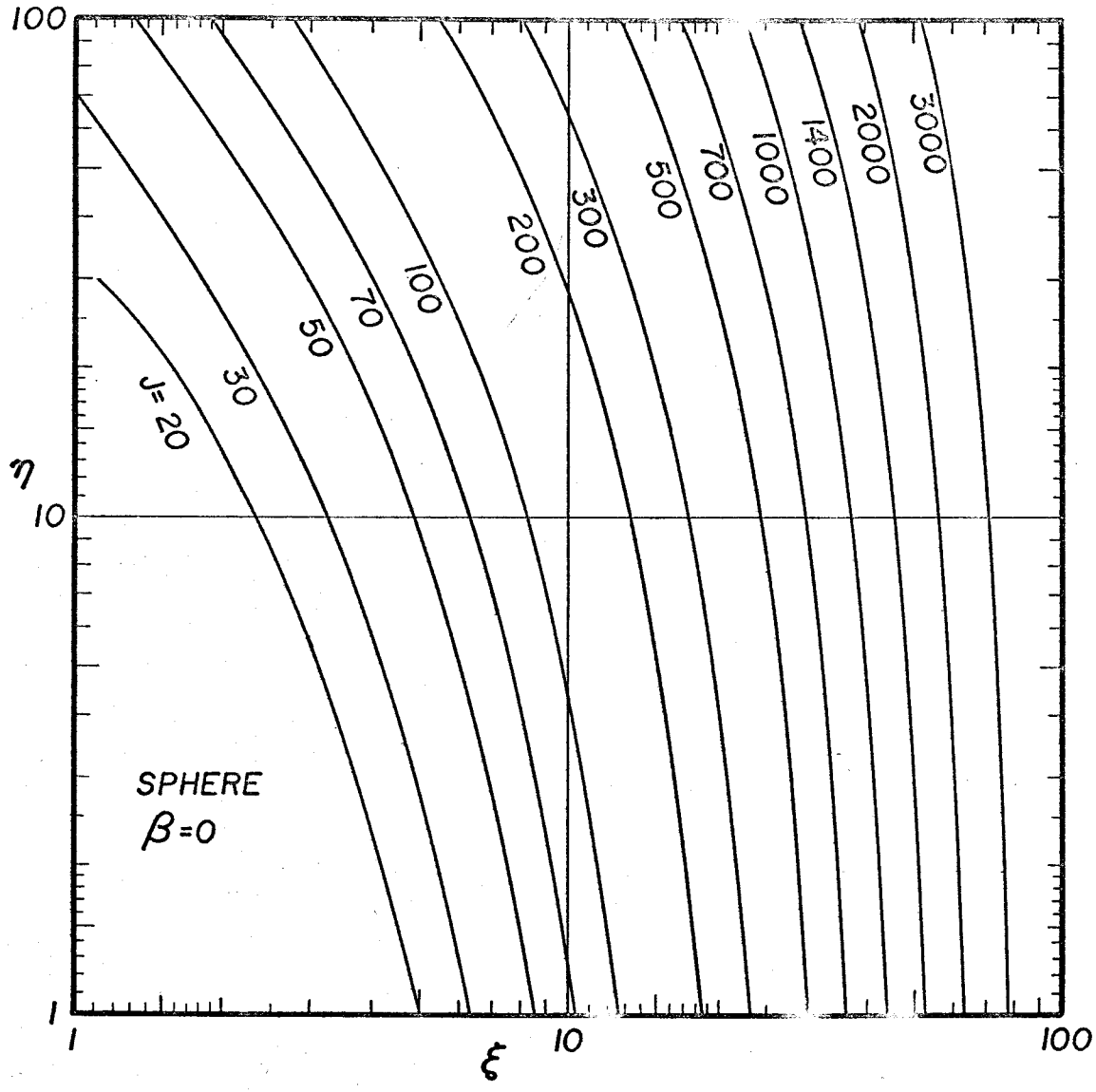
100
10
1
η
1
10
100
ξ
J= 20
30
50
70
100
200
300
500
700
1000
1400
2000
3000
SPHERE
β=0
643119

Figure 2

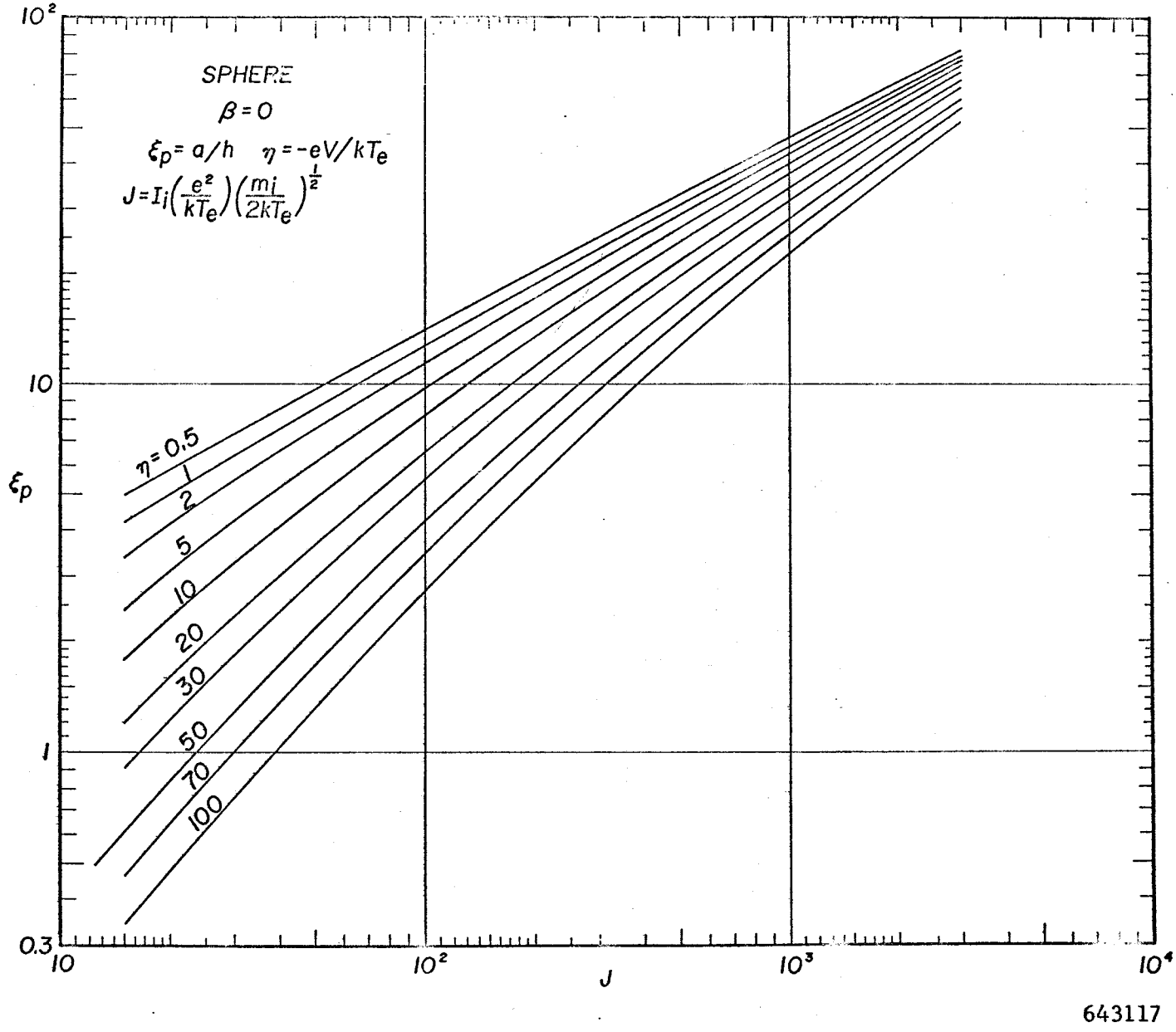
SPHERE
β = 0
ξp = a/h η = -eV/kTe
J = Ii (e²/kTe) (mi/2kTe)^½
η = 0.5
1
2
5
10
20
30
50
70
100
ξp
J
10²
10
1
0.3
10
10²
10³
10⁴
643117

Figure 3

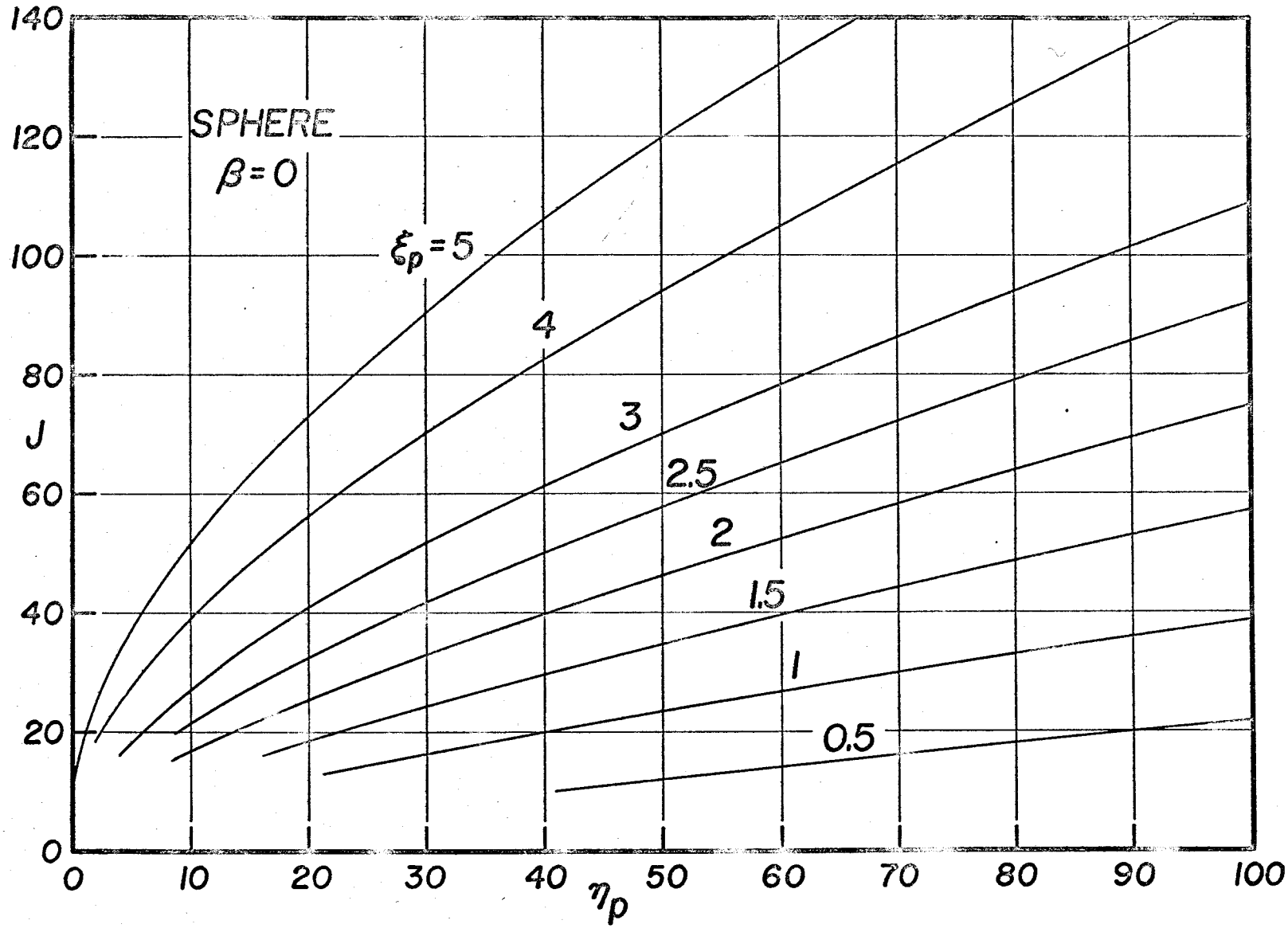

643125

Figure 4a

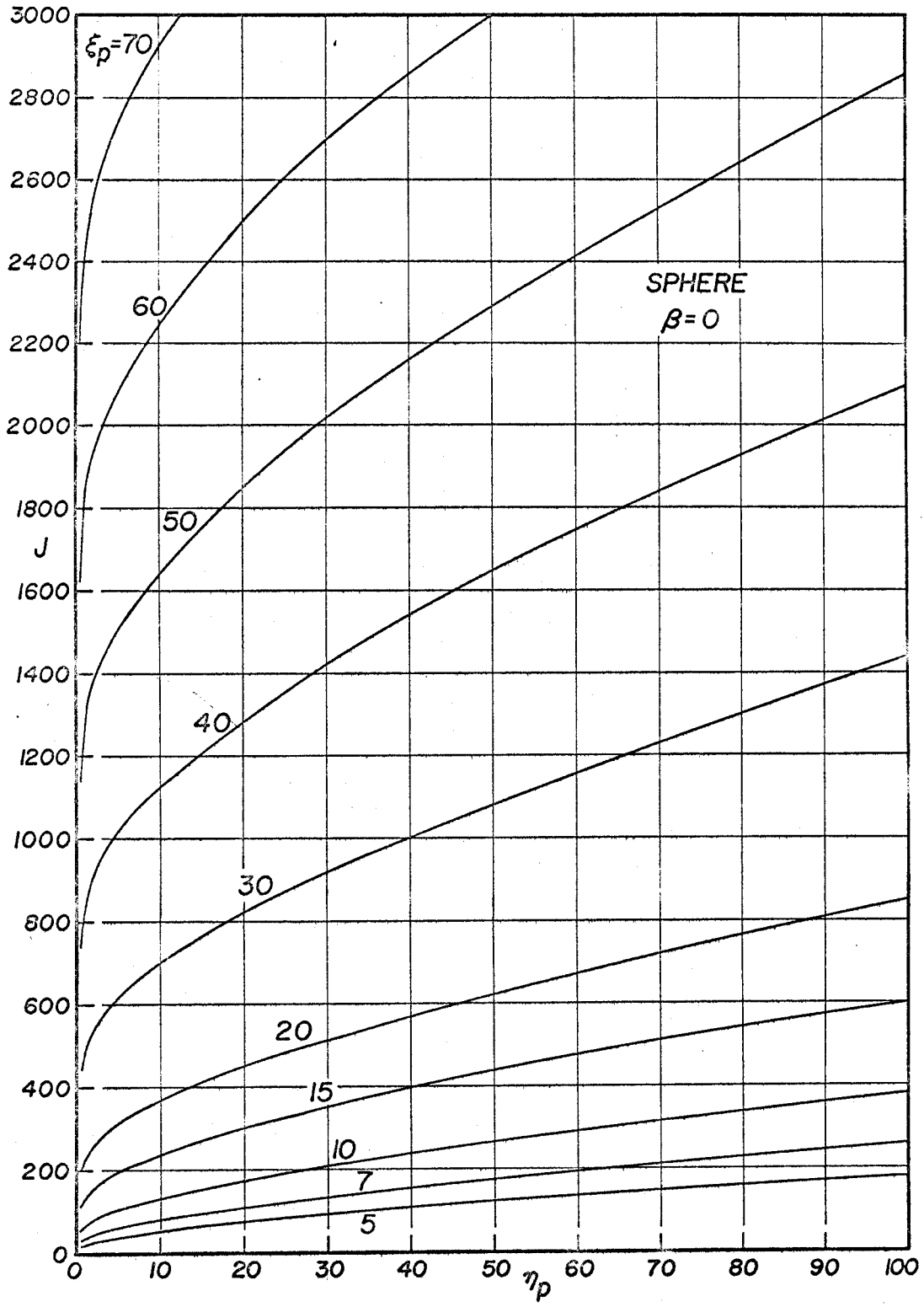

643129

Figure 4b

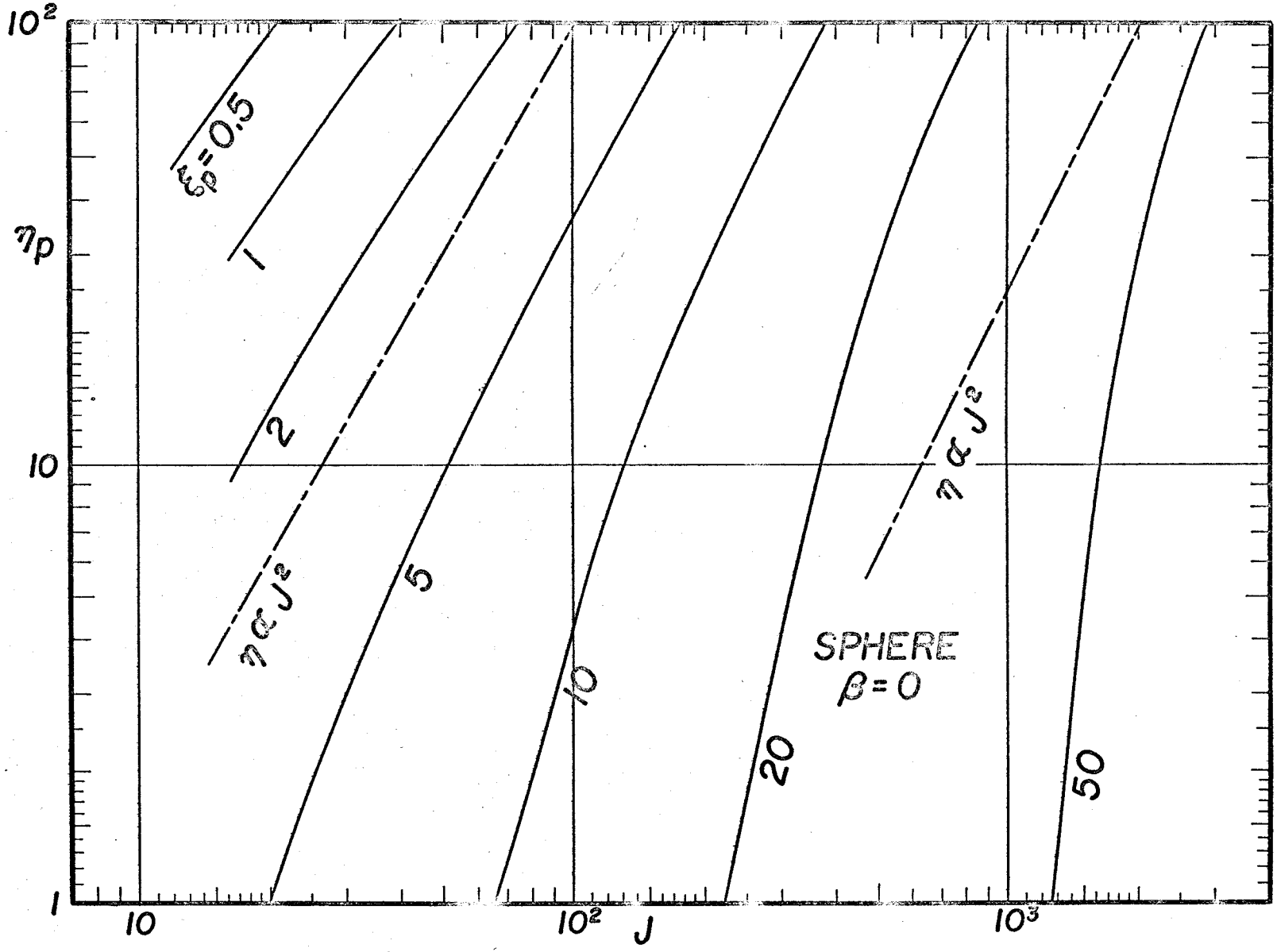

Figure 5

643123

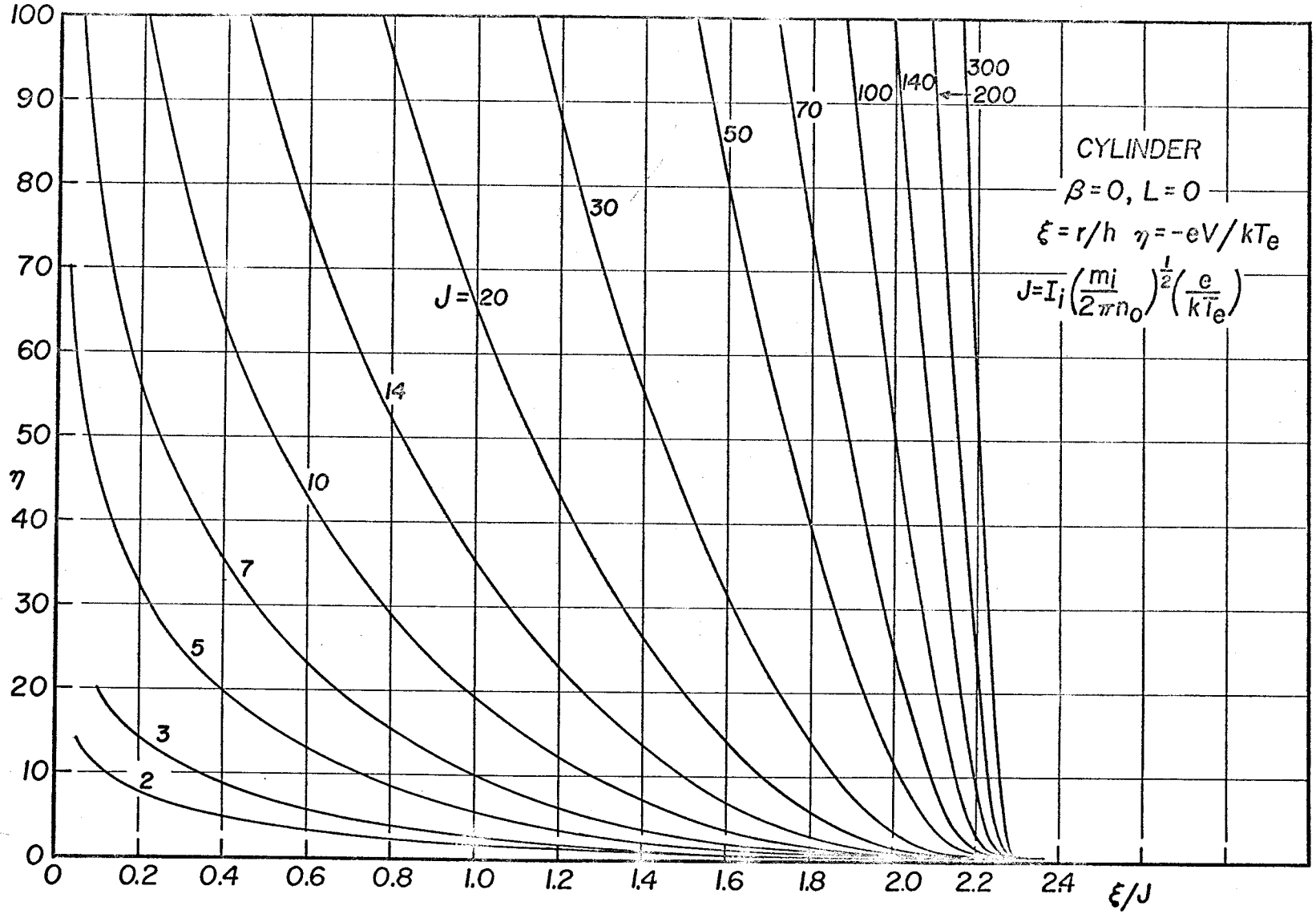

643118

Figure 6

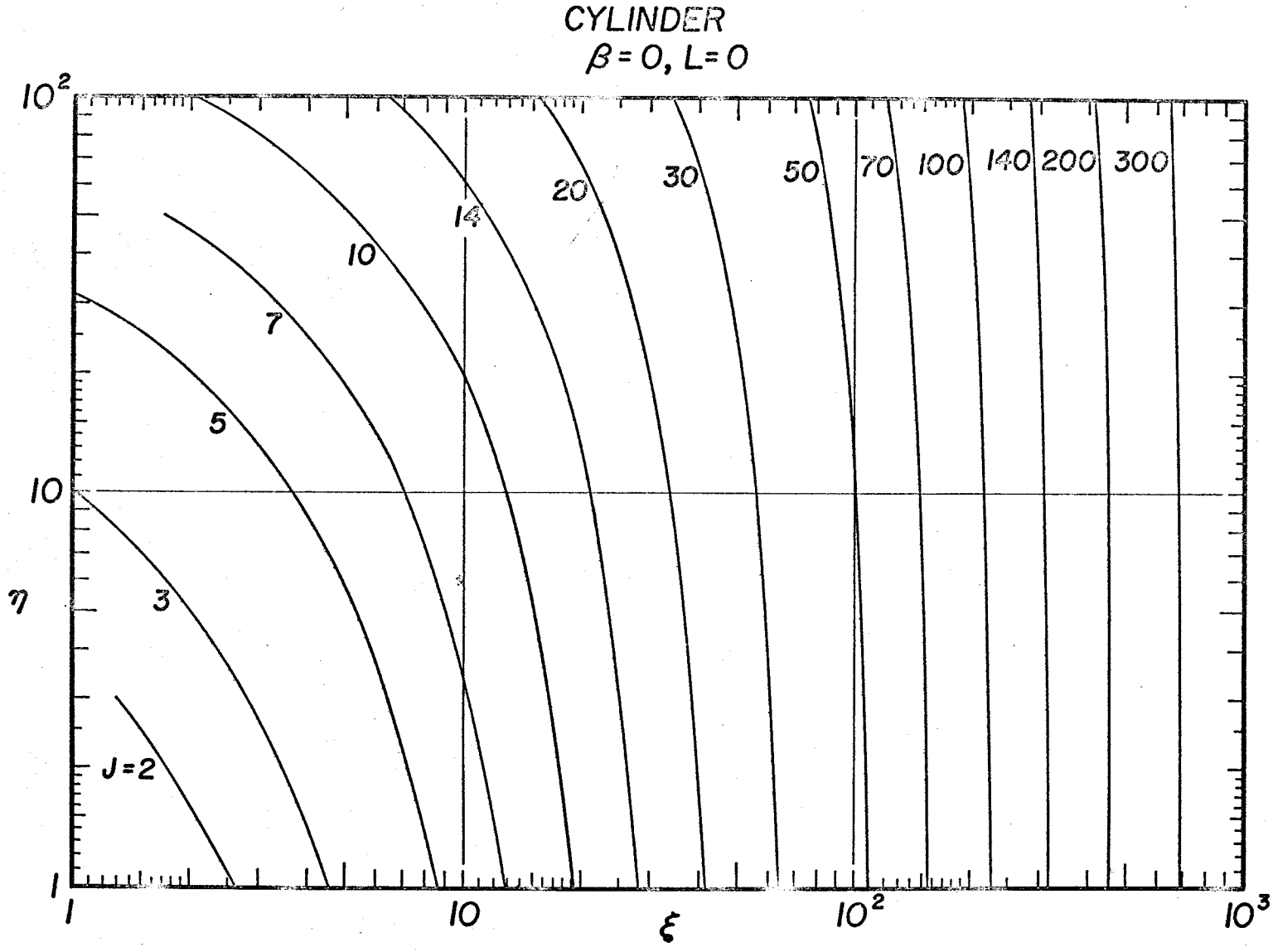

643120

Figure 7

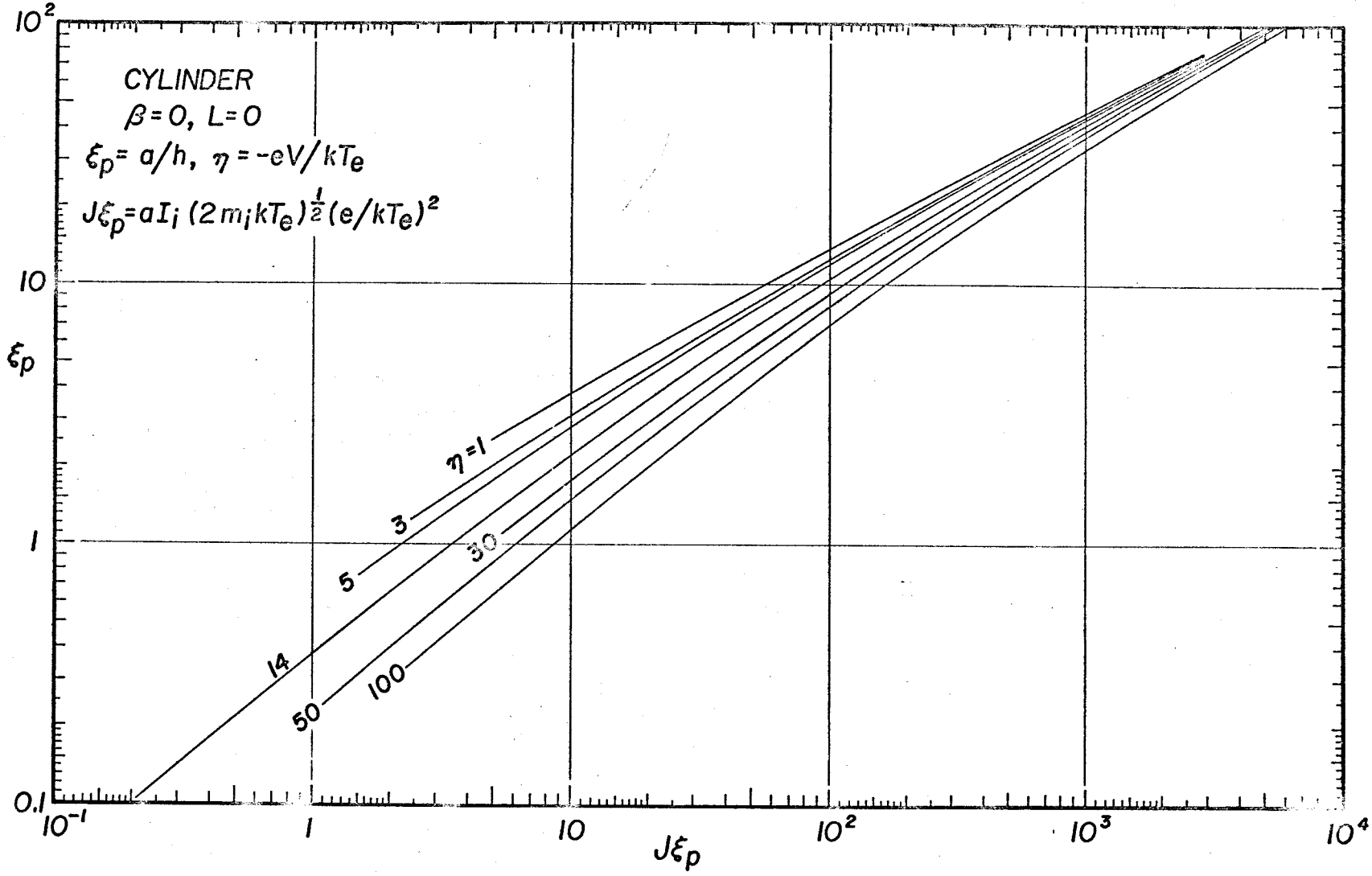

Figure 8

643121

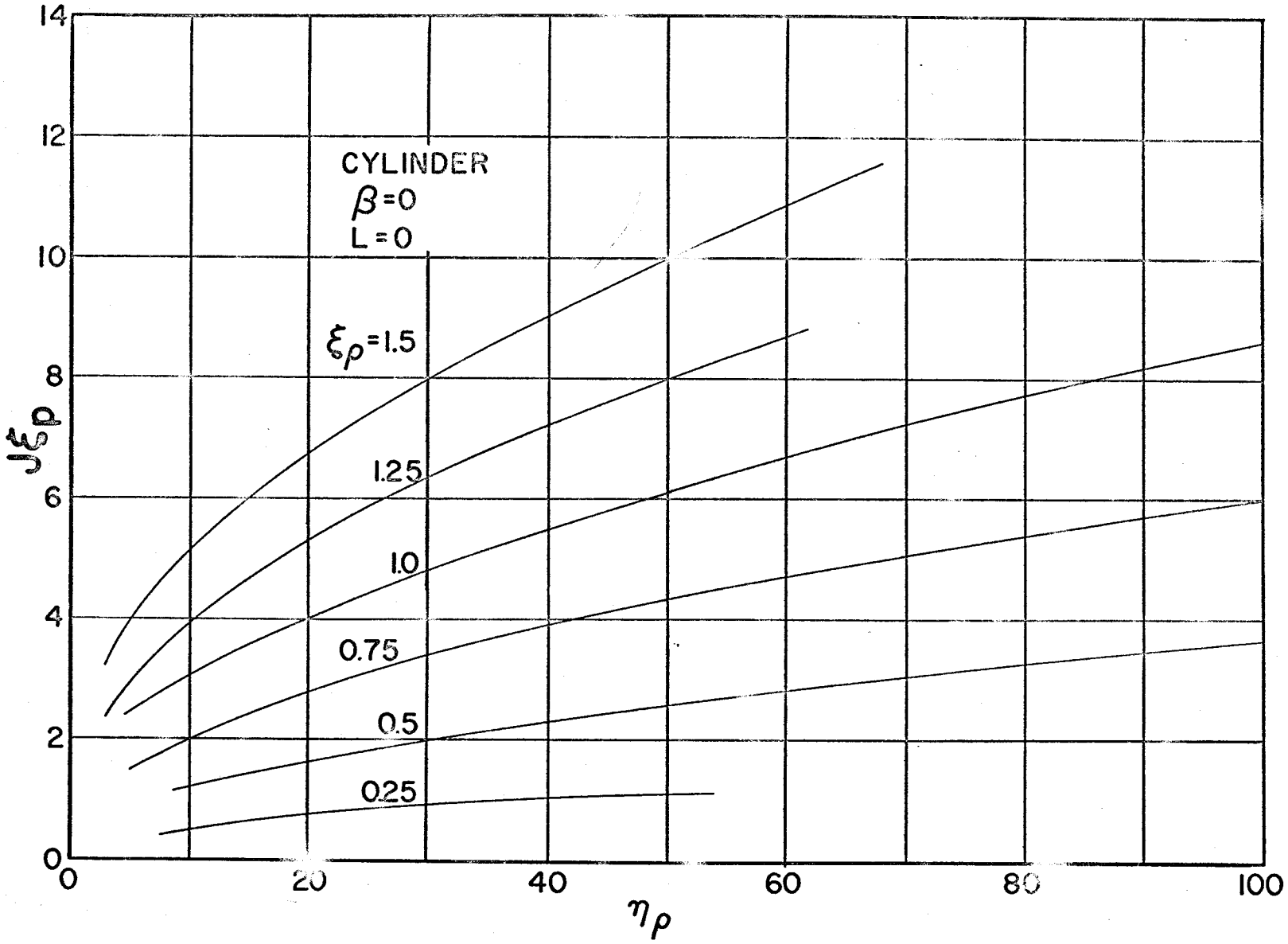

643252

Figure 9a

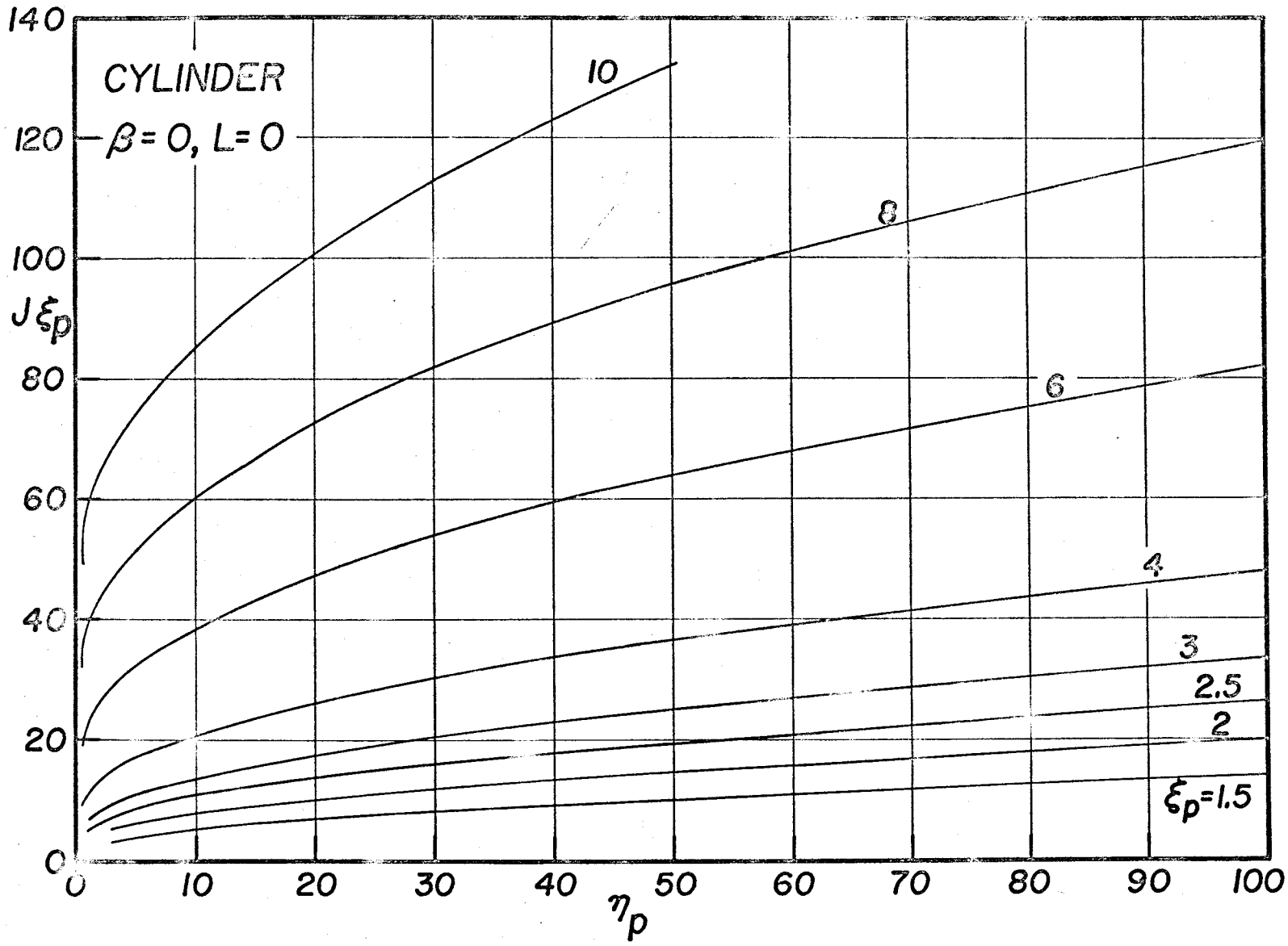

643126

Figure 9b

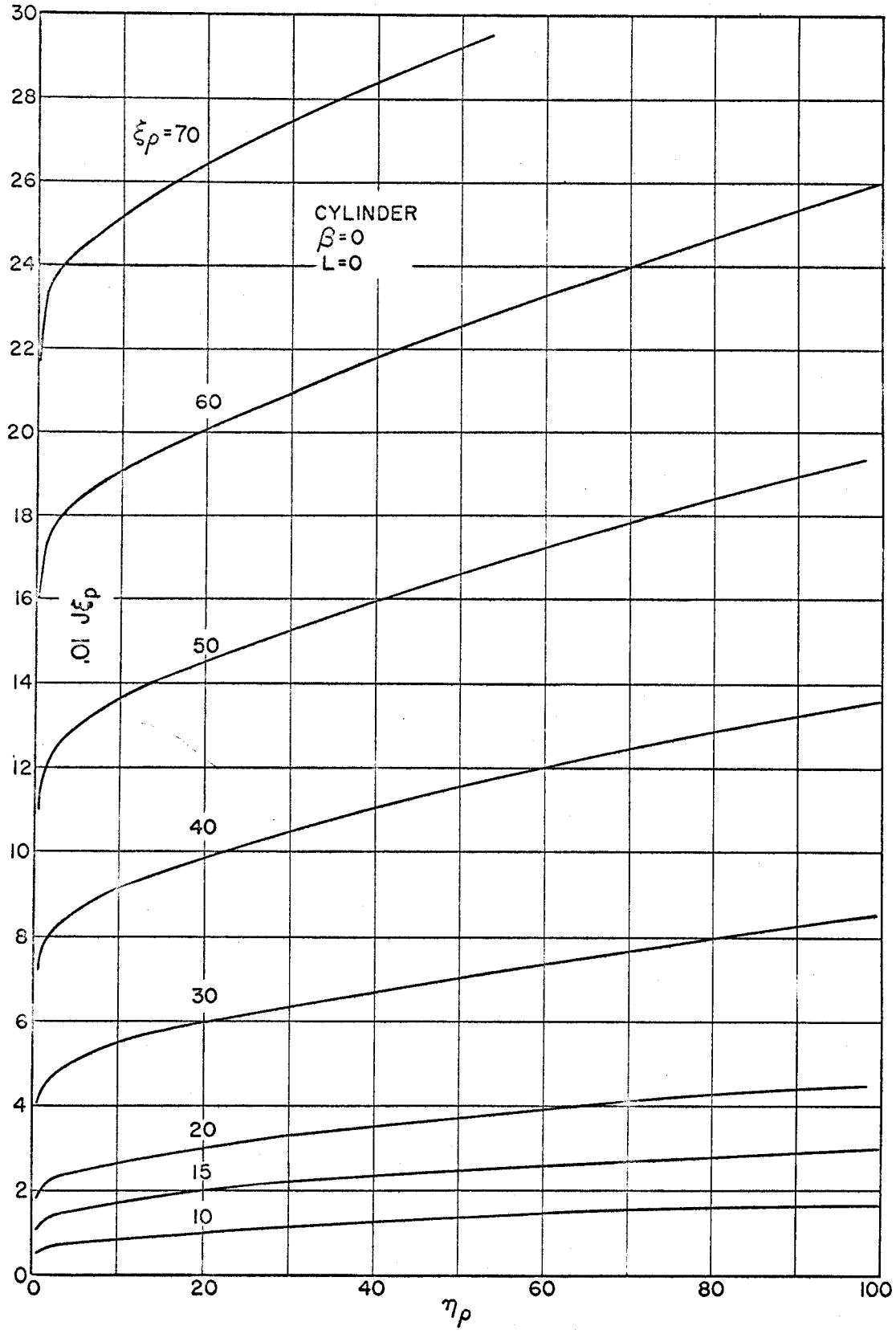

643233

Figure 9c

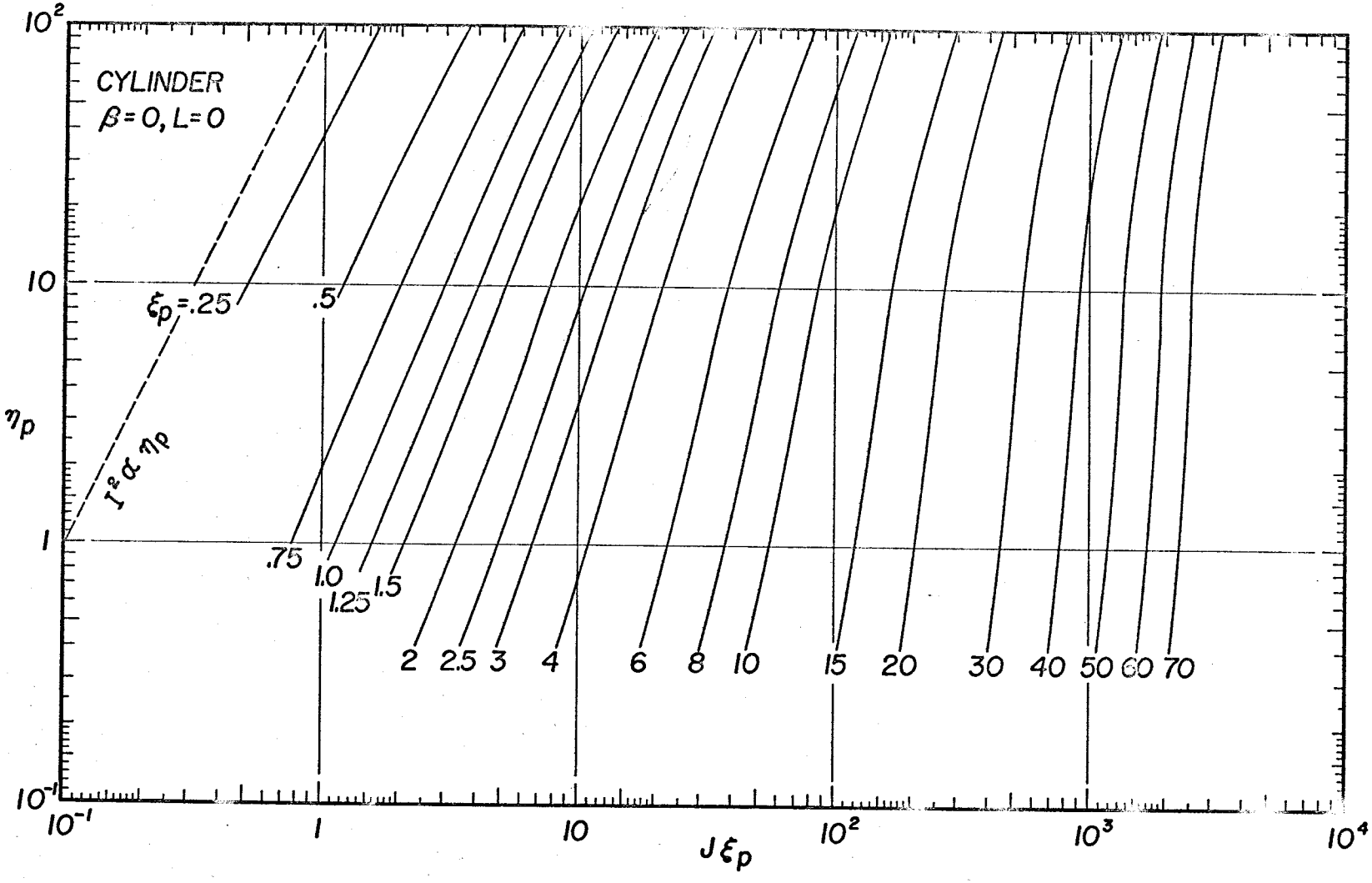

643250

Figure 10

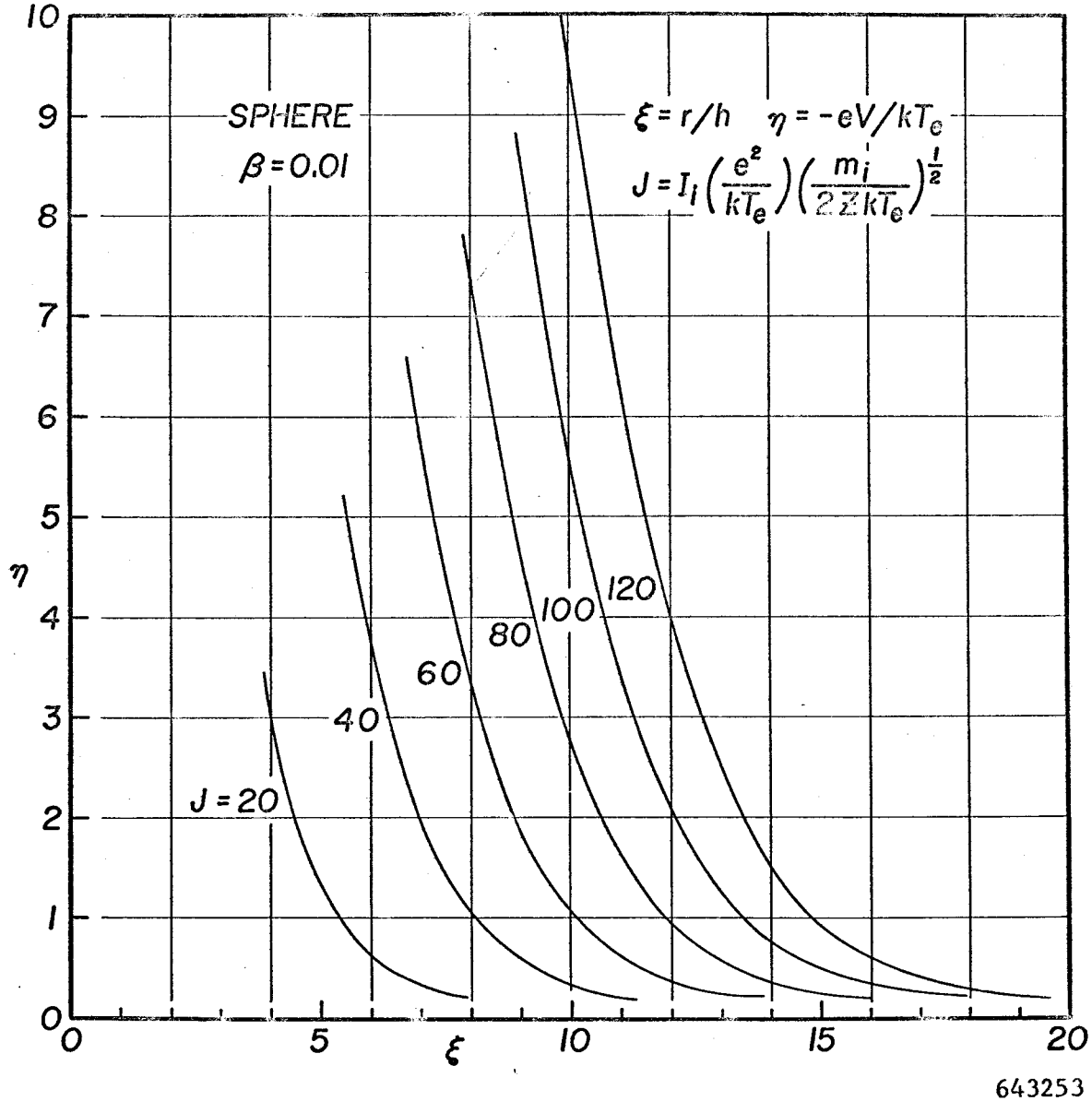
SPHERE
β = 0.01
ξ = r/h
η = -eV/kTe
J = Ii (e²/kTe) (mi/2πkTe)^½
J = 20
40
60
80
100
120
η
ξ
0
5
10
15
20
1
2
3
4
5
6
7
8
9
10
643253

Figure 11a

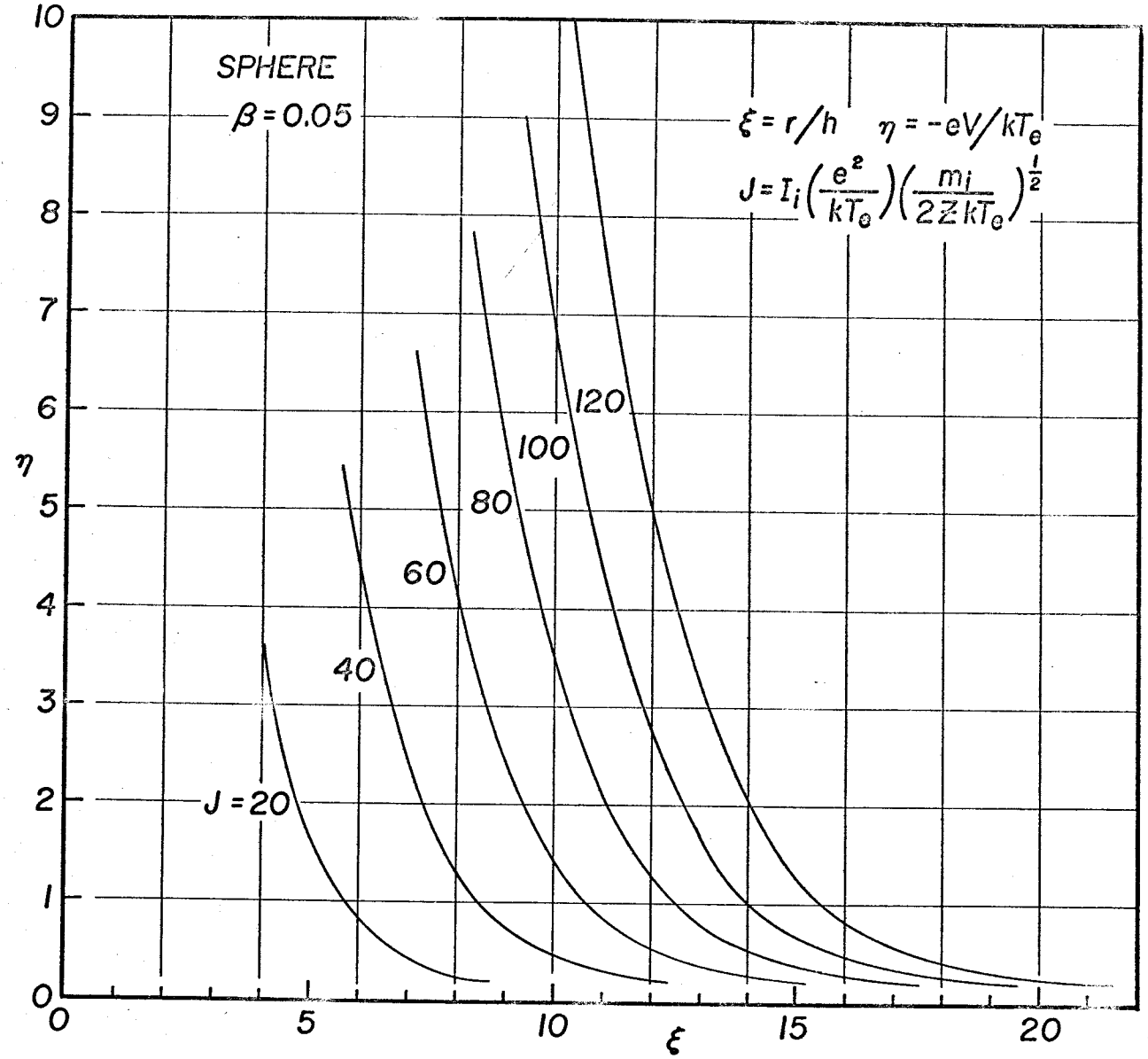

643255

Figure 11b

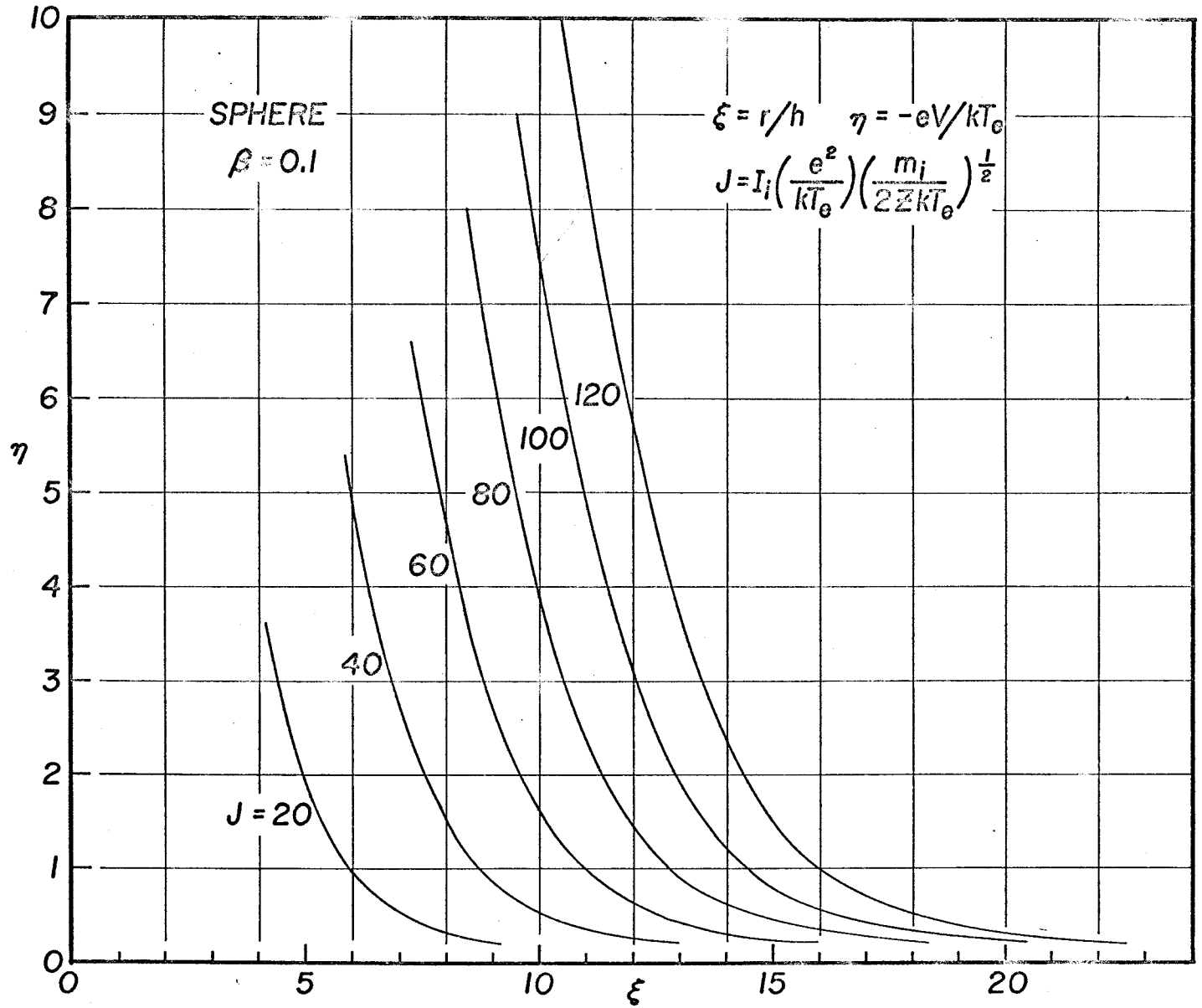
SPHERE
β = 0.1
ξ = r/h
η = -eV/kT_e
J = I_i (e²/kT_e)(m_i/2πkT_e)^½
120
100
80
60
40
J = 20
η
ξ
0
5
10
15
20
1
2
3
4
6
7
8
9
643254

Figure 11c

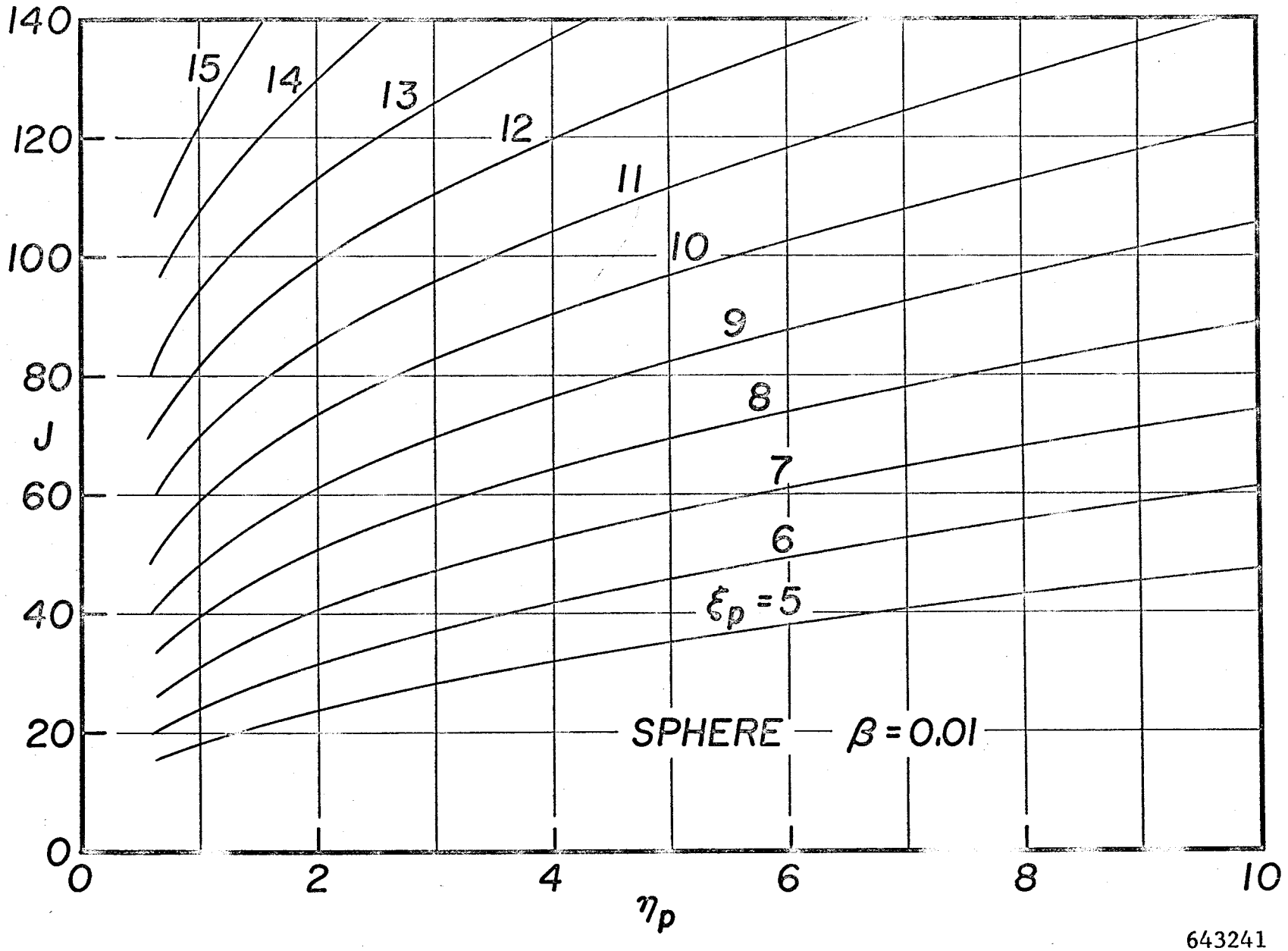
140
120
100
80
60
40
20
0
J
0
2
4
6
8
10
η_p
15
14
13
12
11
10
9
8
7
6
$\xi_p = 5$
SPHERE
$\beta = 0.01$
643241

Figure 12a

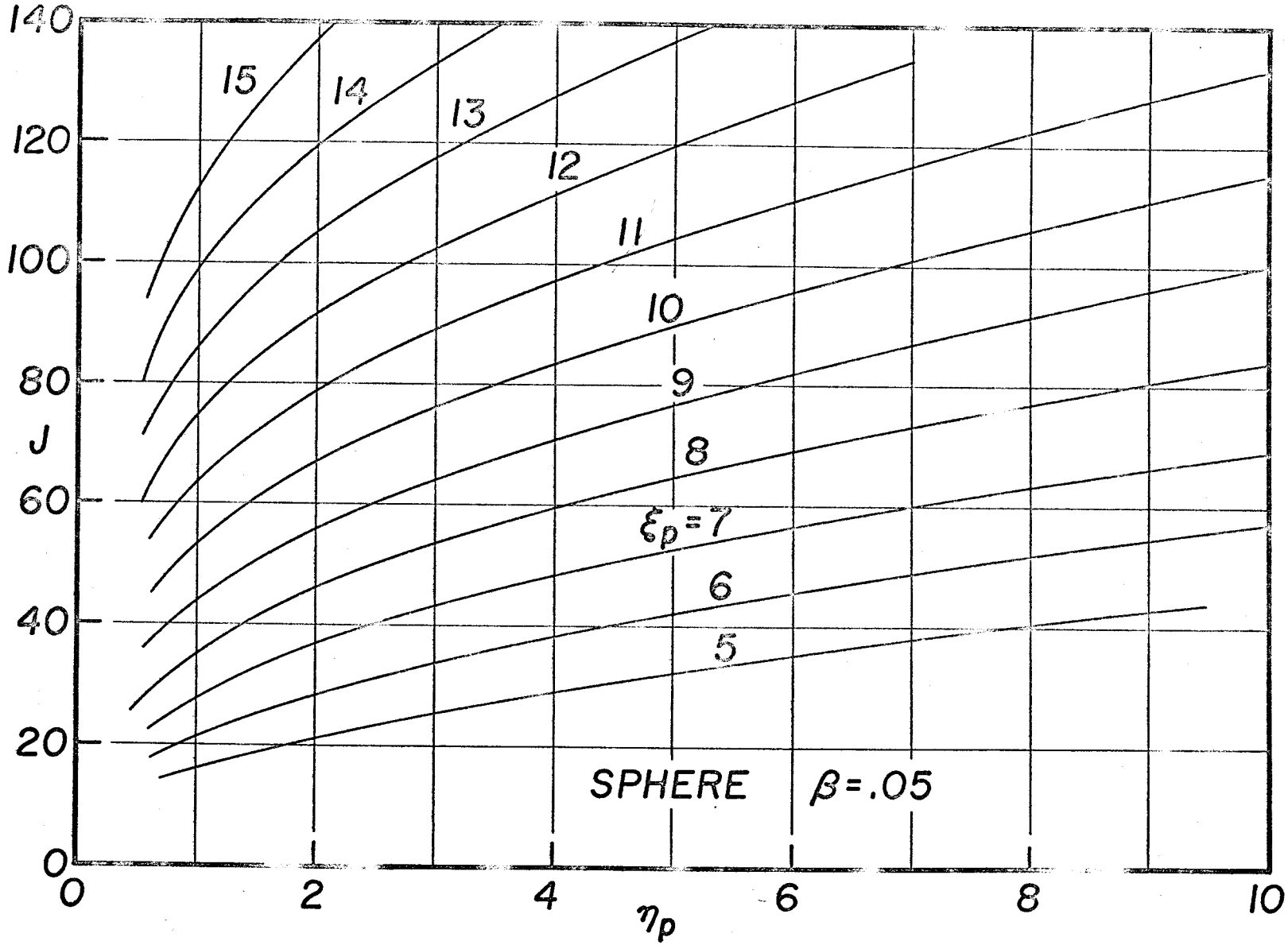

643246

Figure 12b

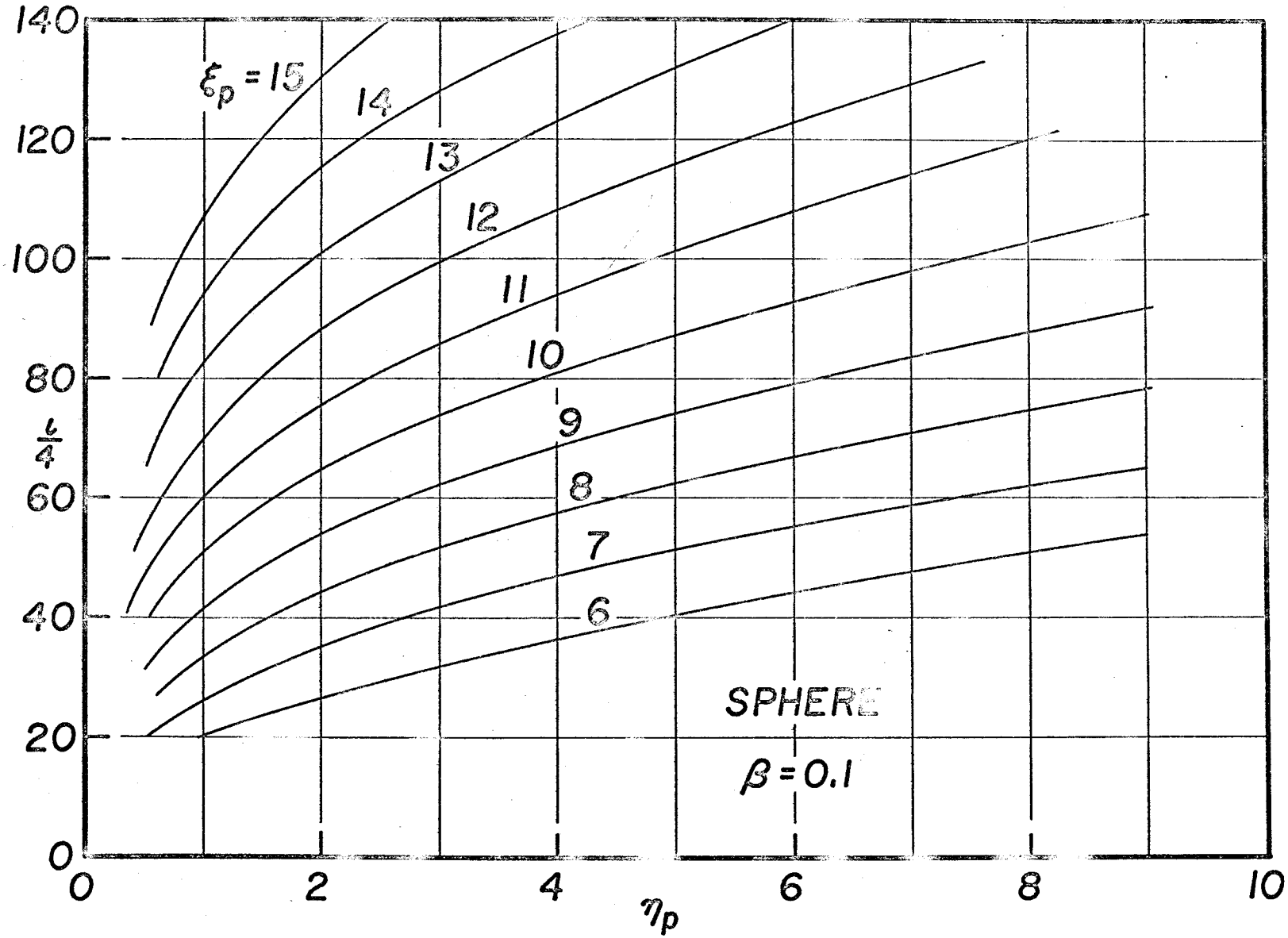

643196

Figure 12c

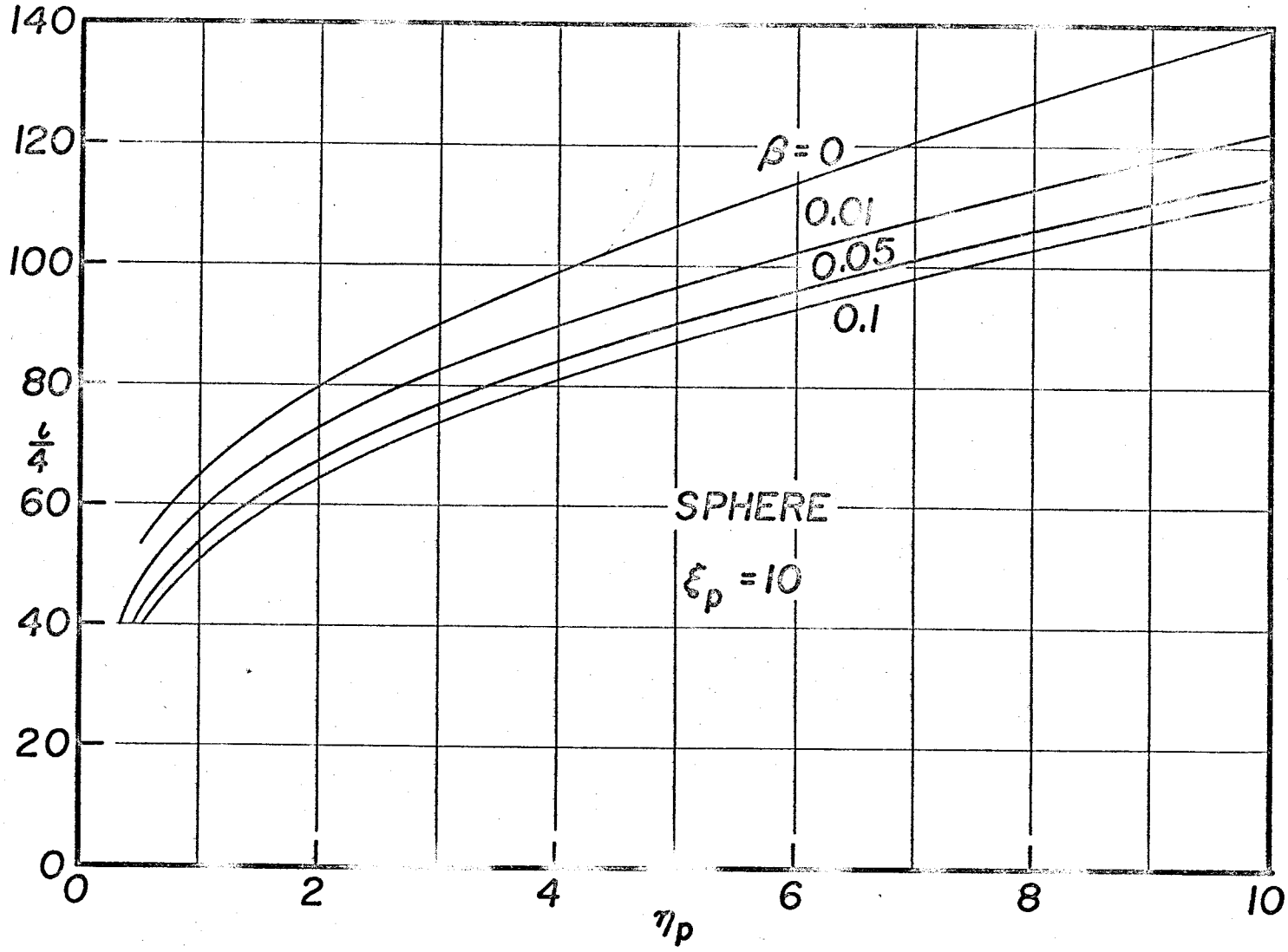

643198

Figure 13

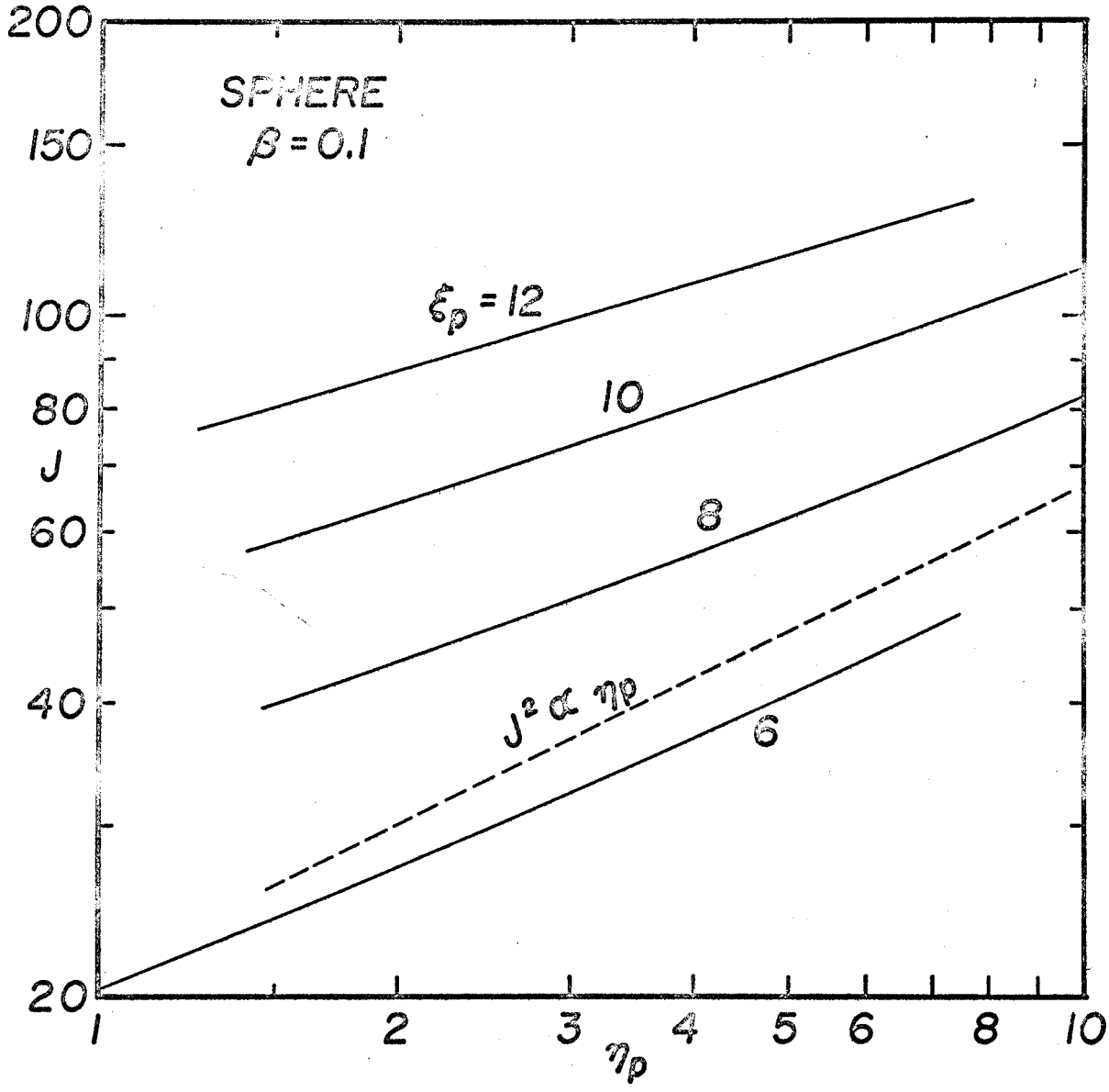
200
150
100
80
60
40
20
J
SPHERE
β = 0.1
ε_p = 12
10
8
6
J² ∝ η_p
1
2
3
4
5
6
8
10
η_p
643245

Figure 14

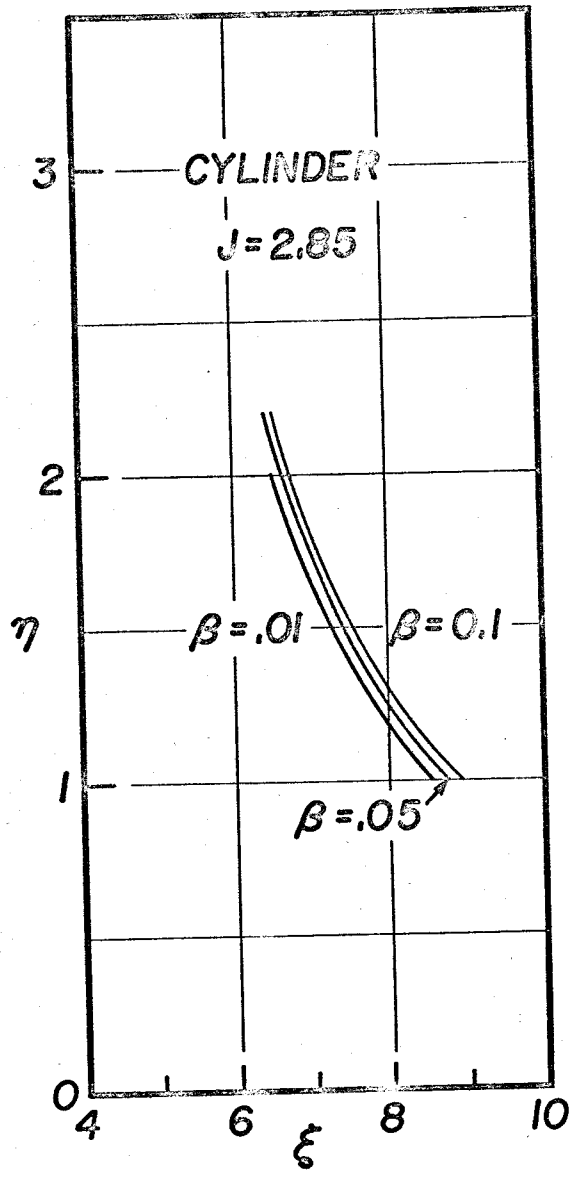

Figure 15a

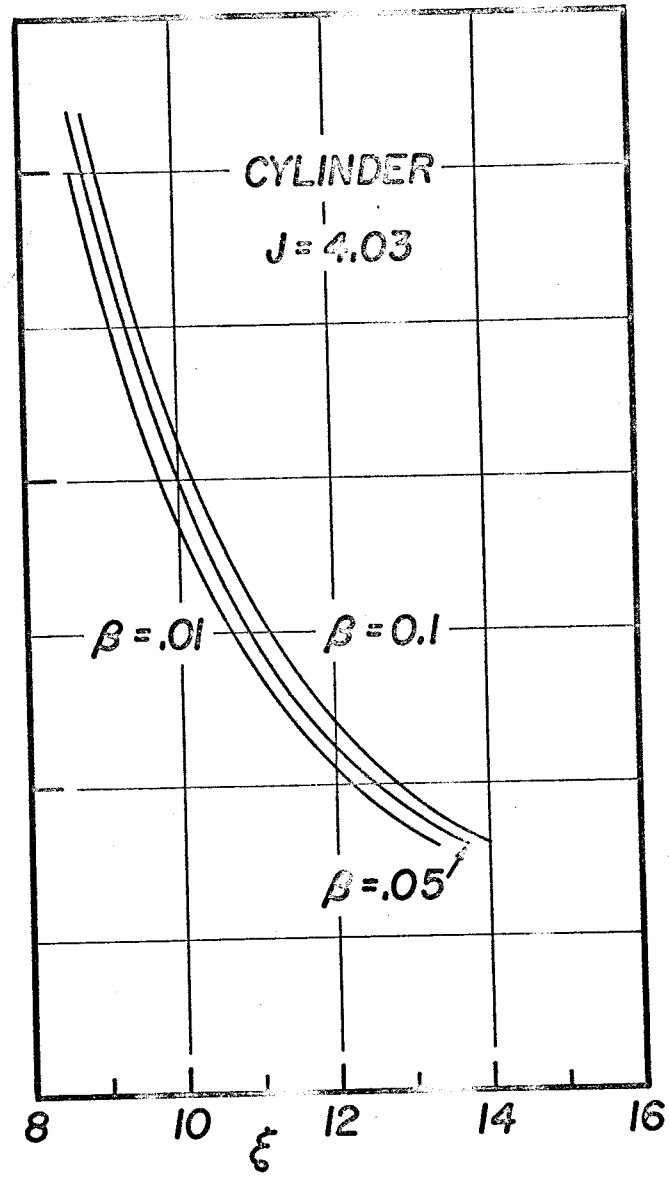

643243

Figure 15b

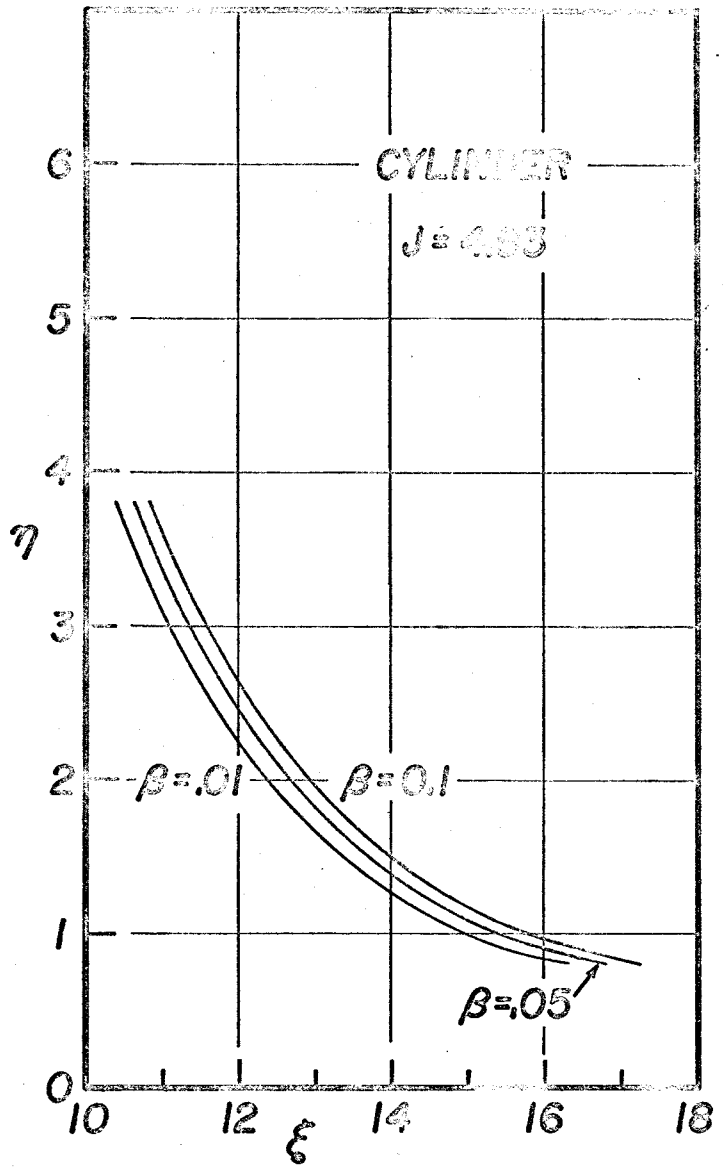

Figure 15c

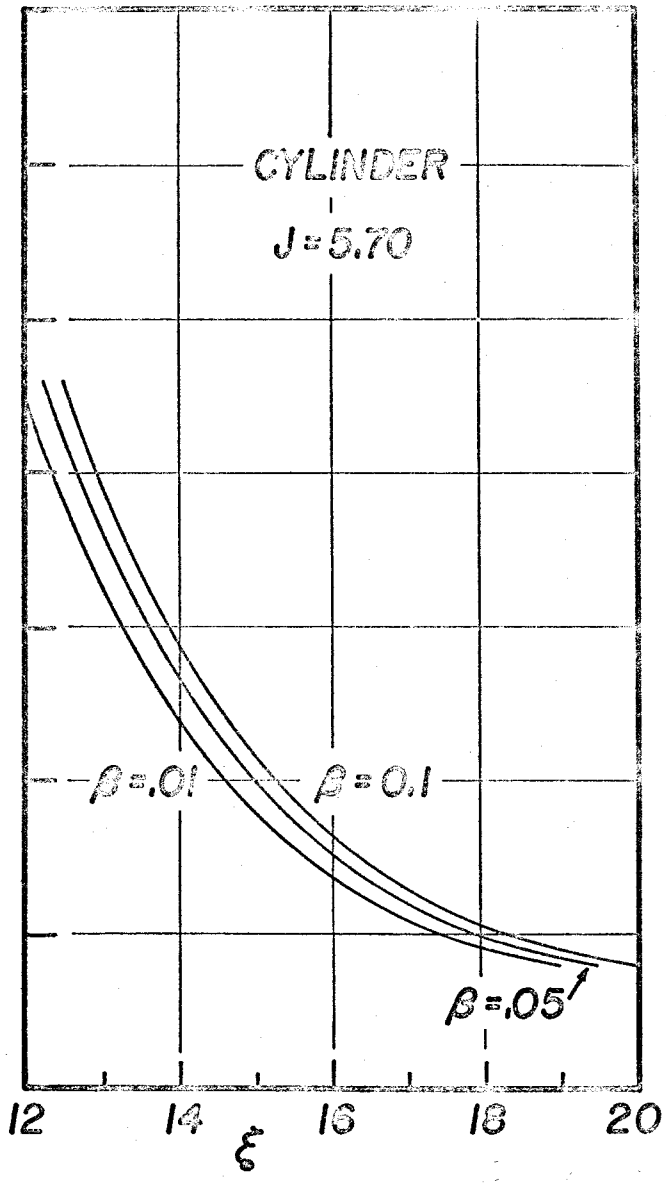

643242

Figure 15d

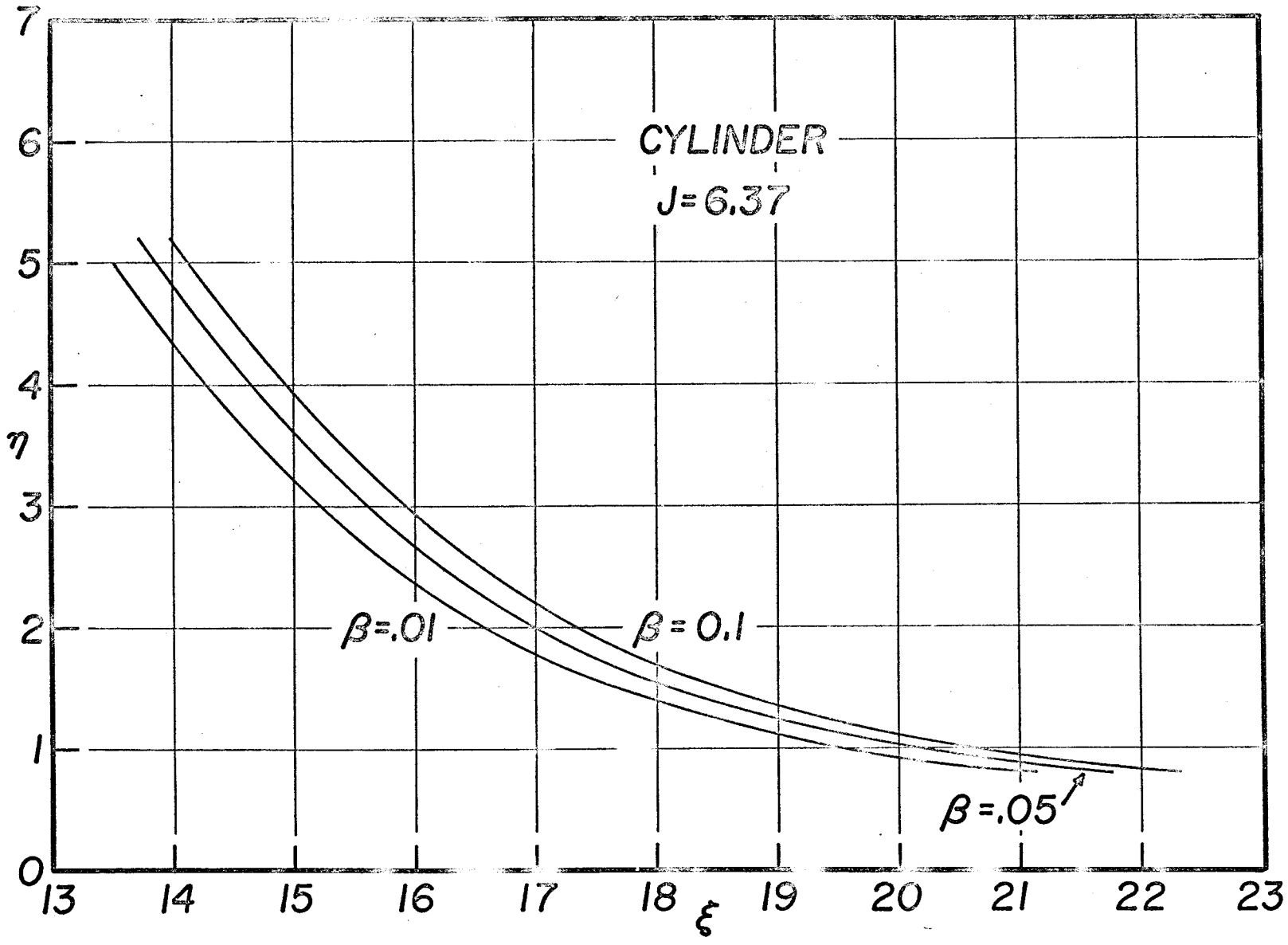

643251

Figure 15e

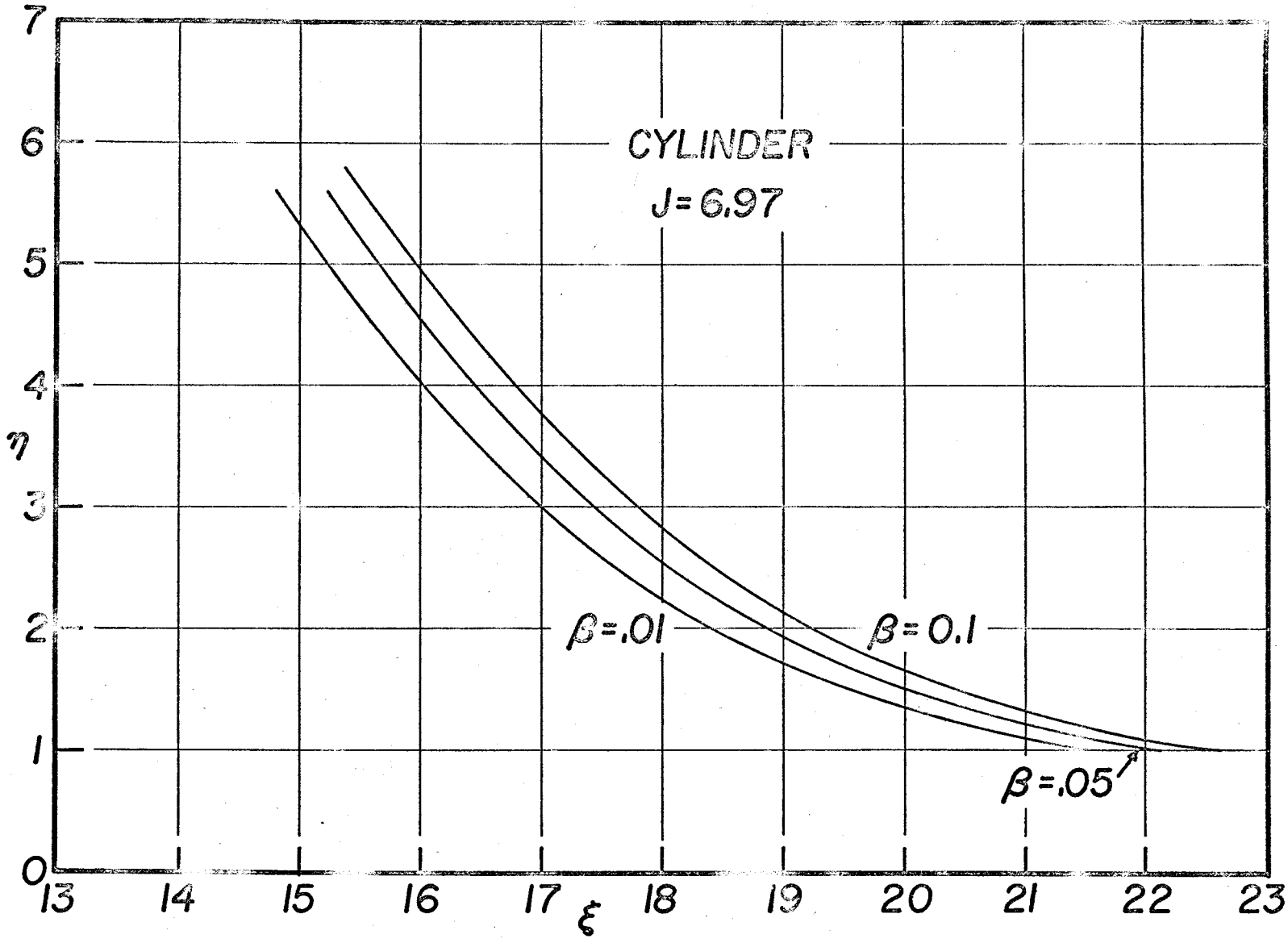

643244

Figure 15f

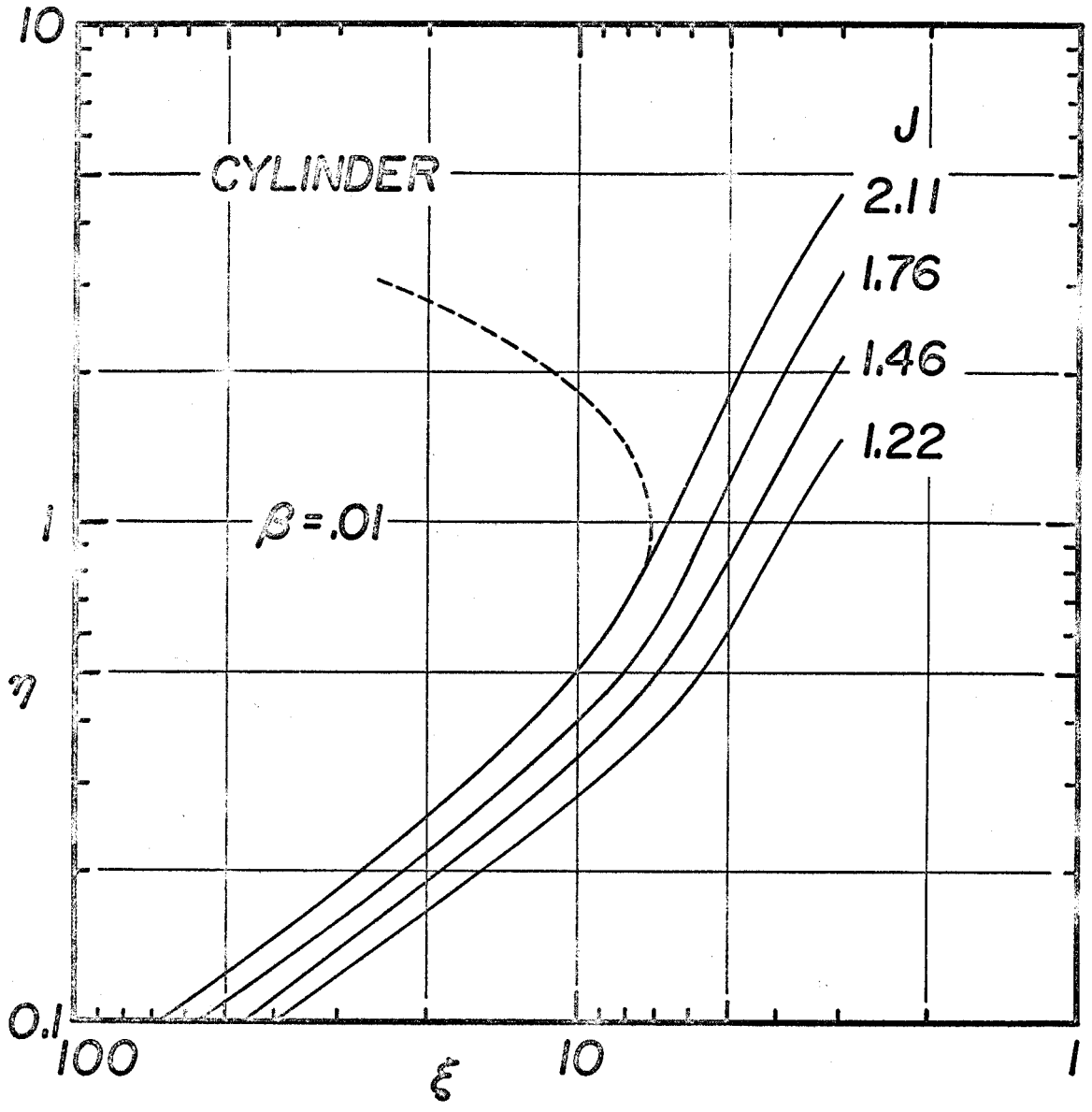

Figure 16a

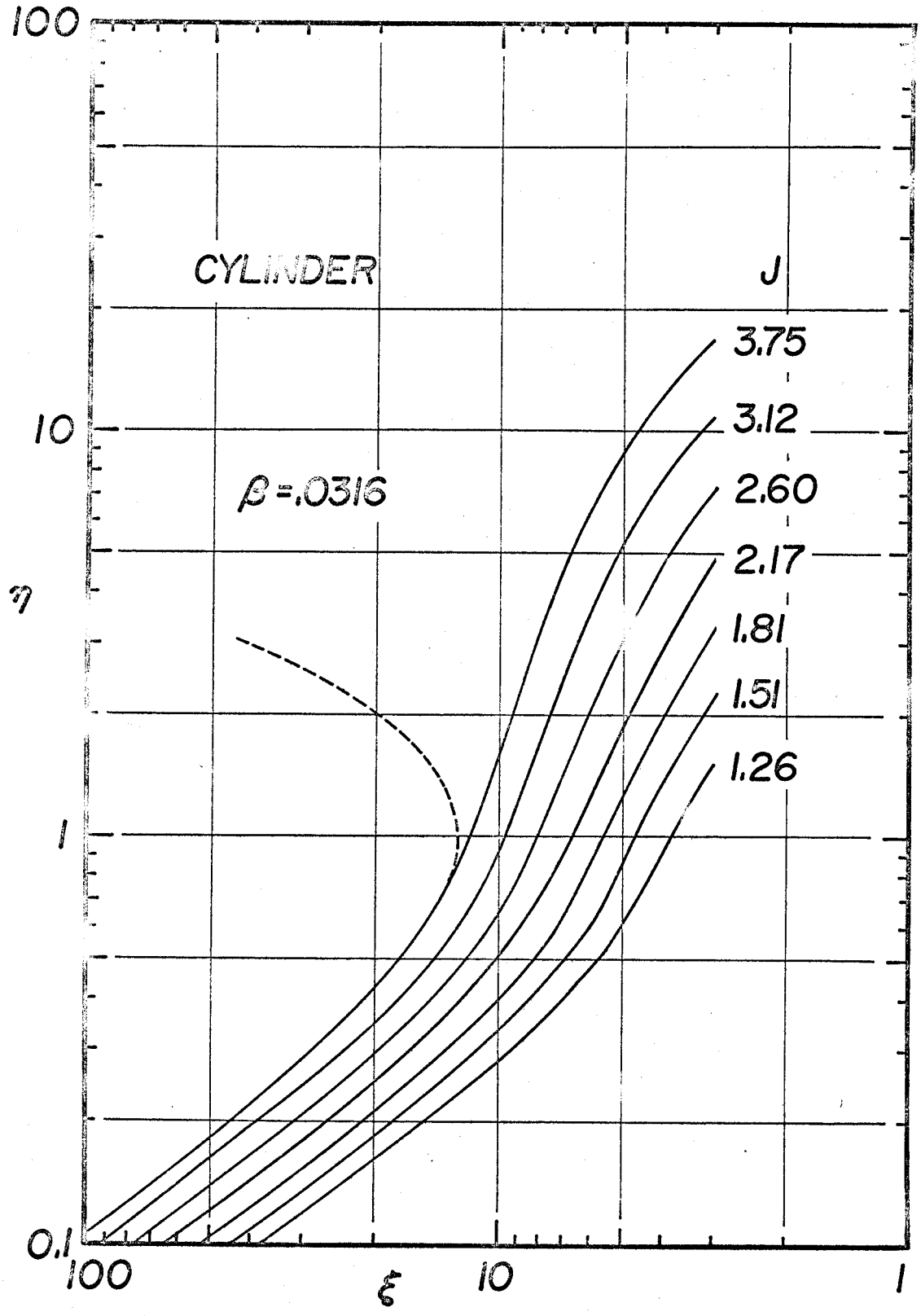

643249

Figure 16b

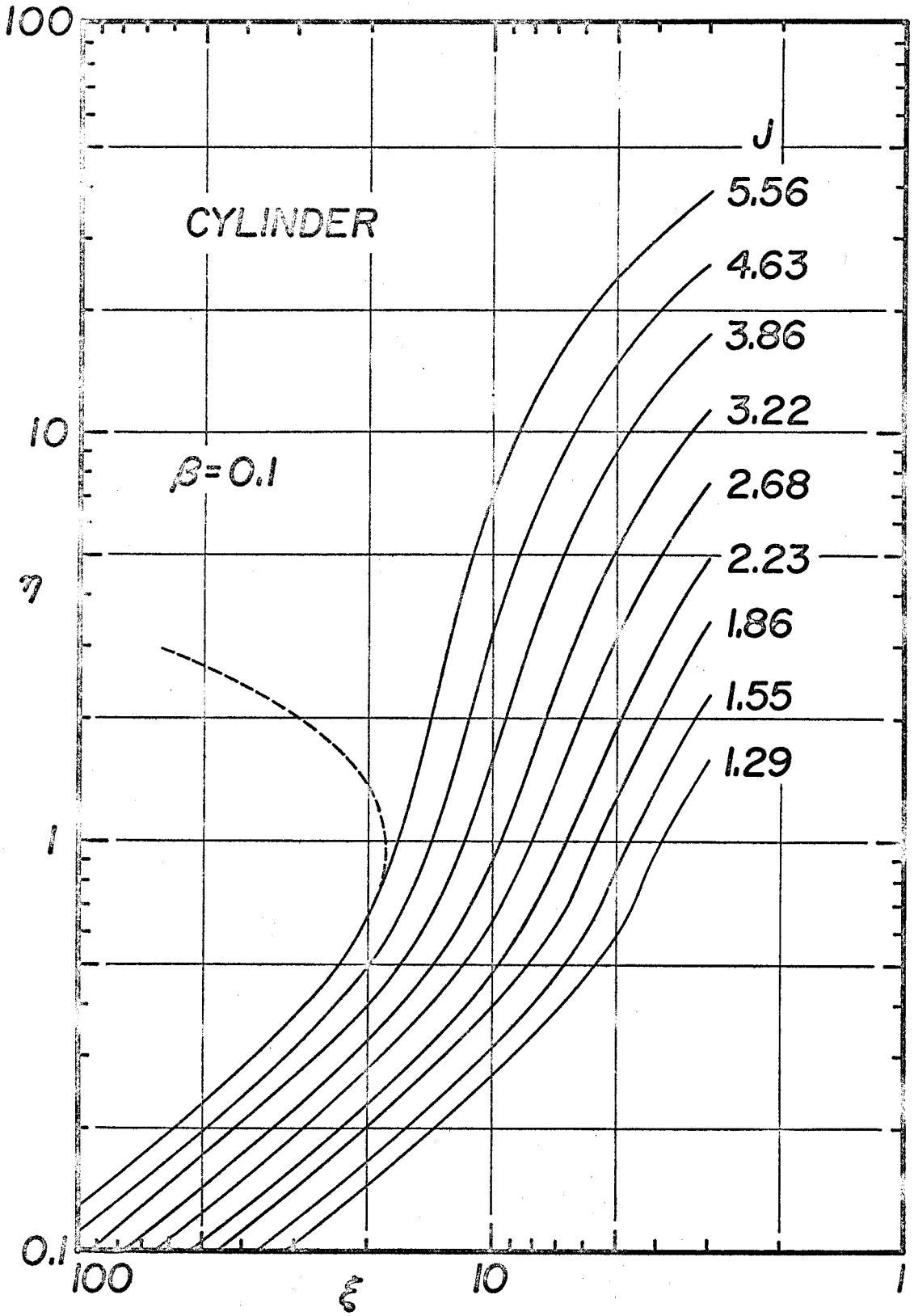
100
10
1
0.1
η
100
10
1
ε
CYLINDER
β=0.1
J
5.56
4.63
3.86
3.22
2.68
2.23
1.86
1.55
1.29
643247

Figure 16c

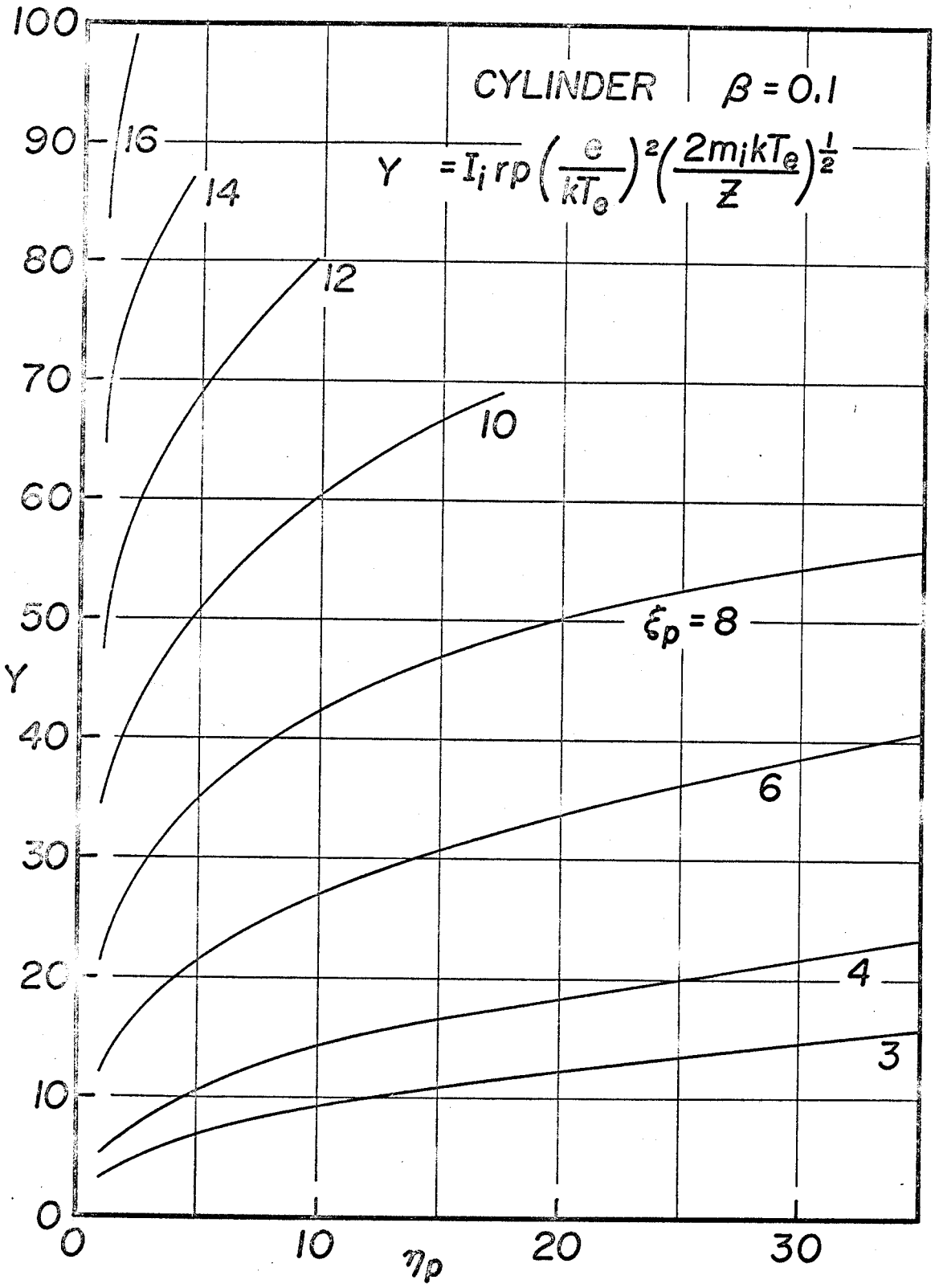

643197

Figure 17

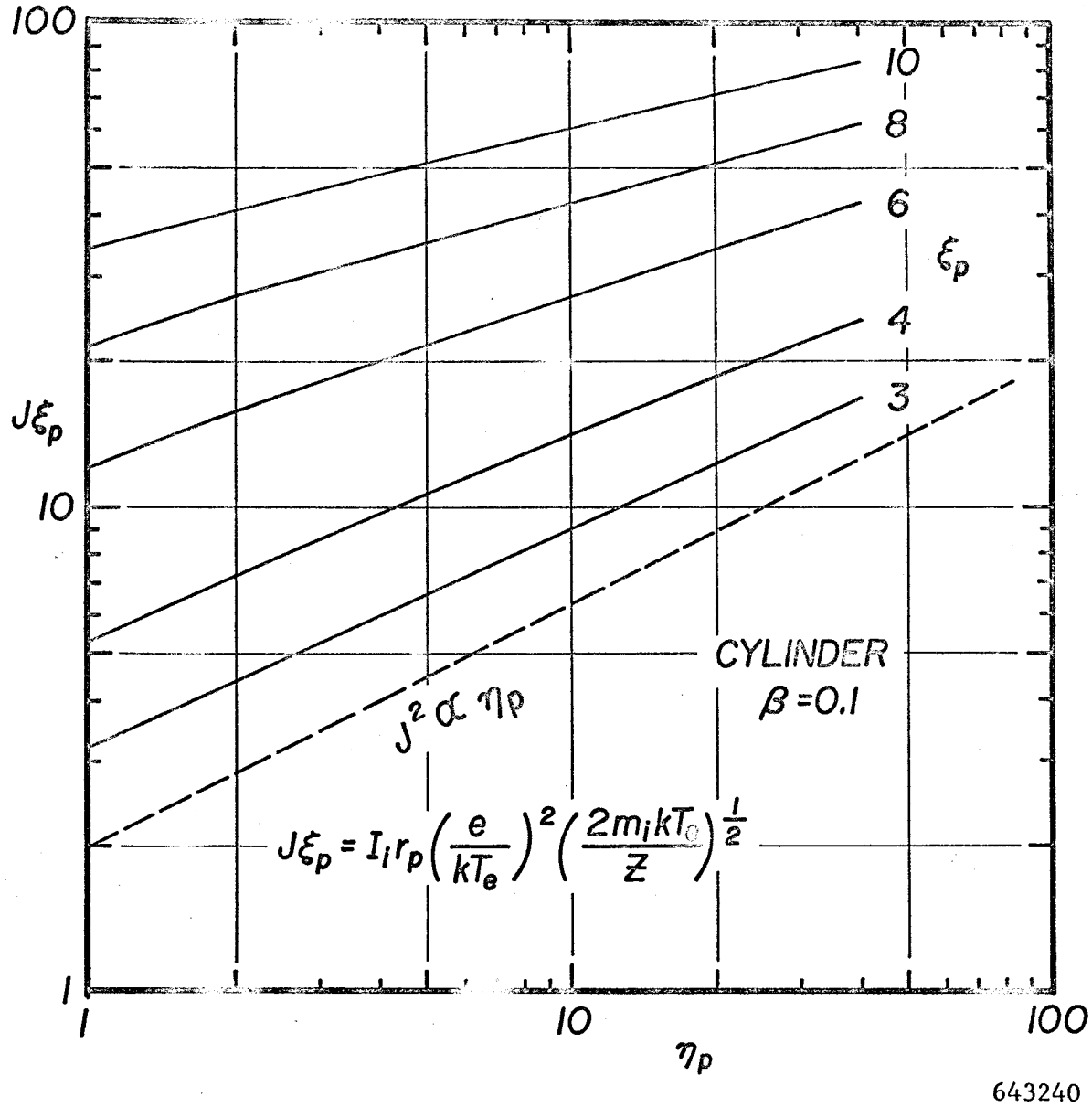
100
10
1
1
10
100
$J\xi_p$
η_p
10
8
6
4
3
ξ_p
CYLINDER
$\beta = 0.1$
$J^2 \propto \eta_p$
$J\xi_p = I_1 r_p \left(\frac{e}{kT_e}\right)^2 \left(\frac{2m_i kT_0}{Z}\right)^{\frac{1}{2}}$
643240

Figure 18

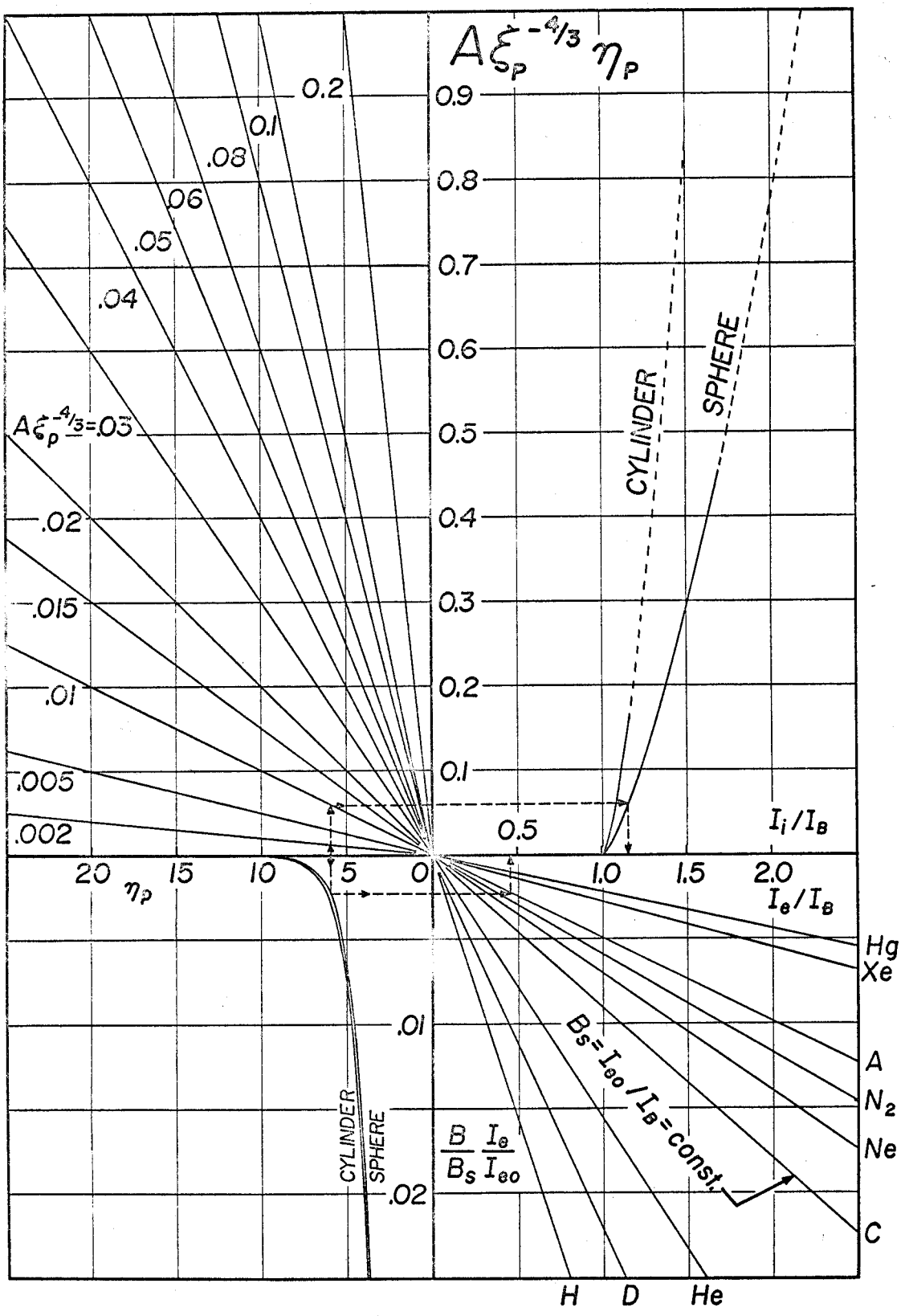

643082

Figure 19

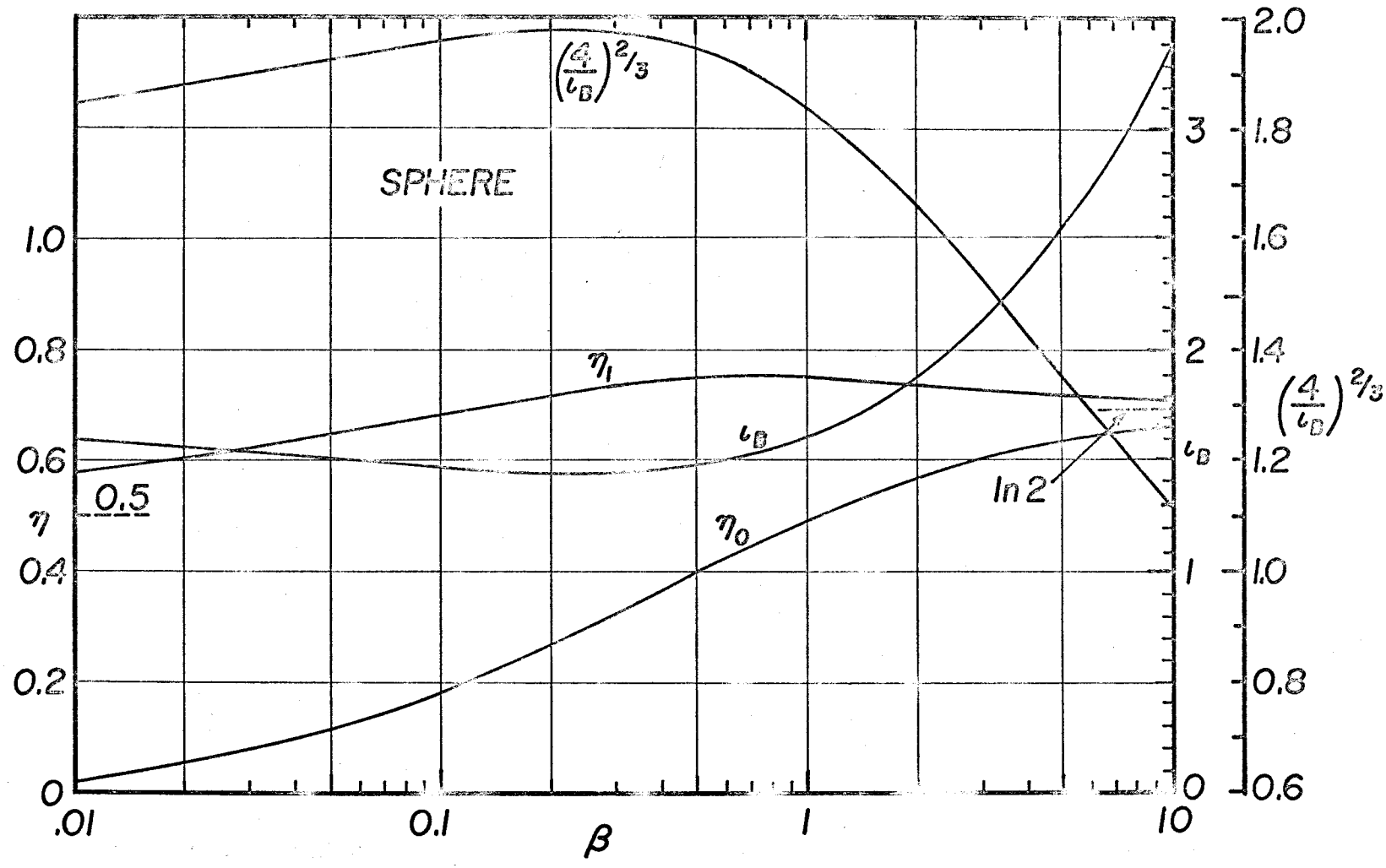

643080

Figure 20

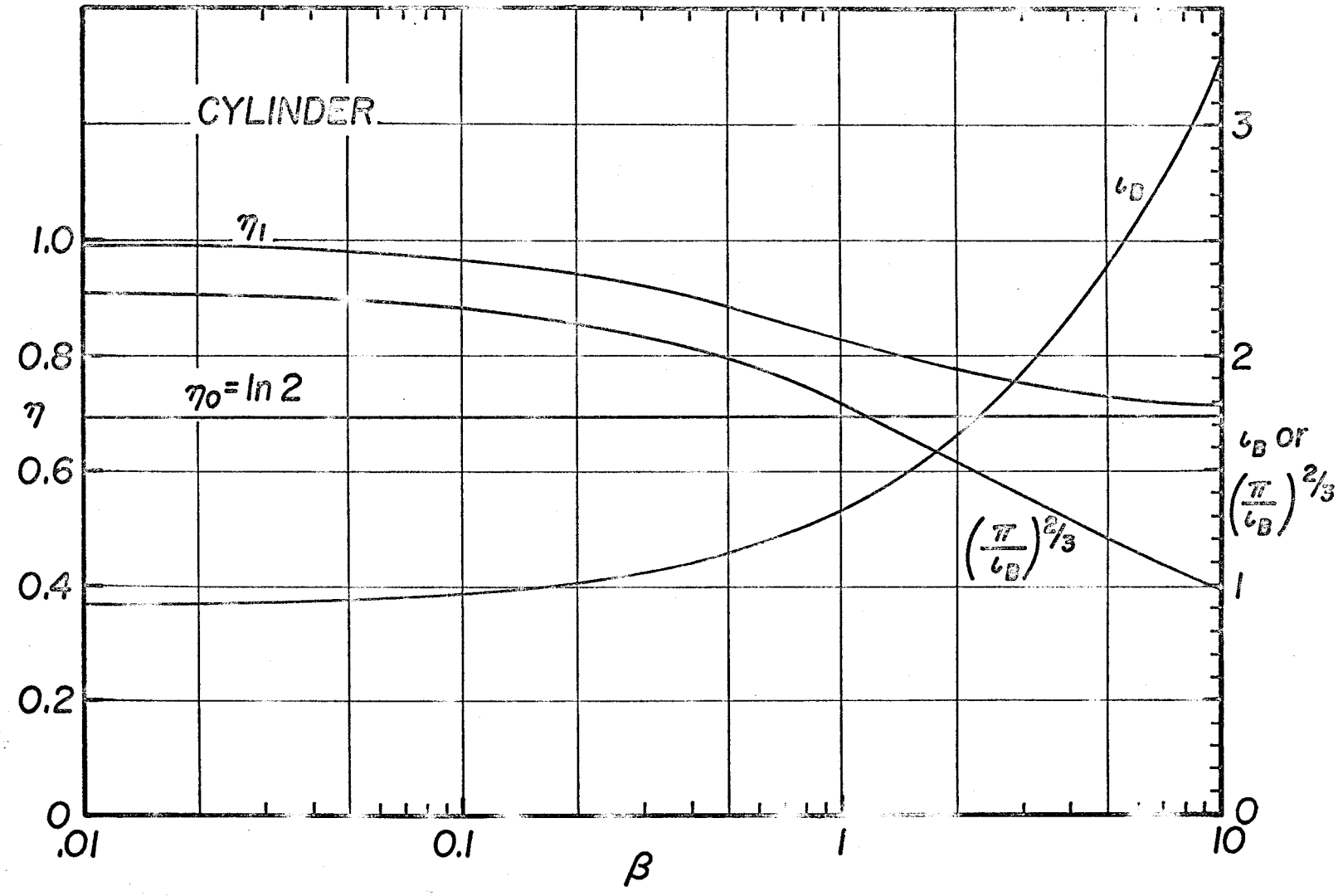

643079

Figure 21

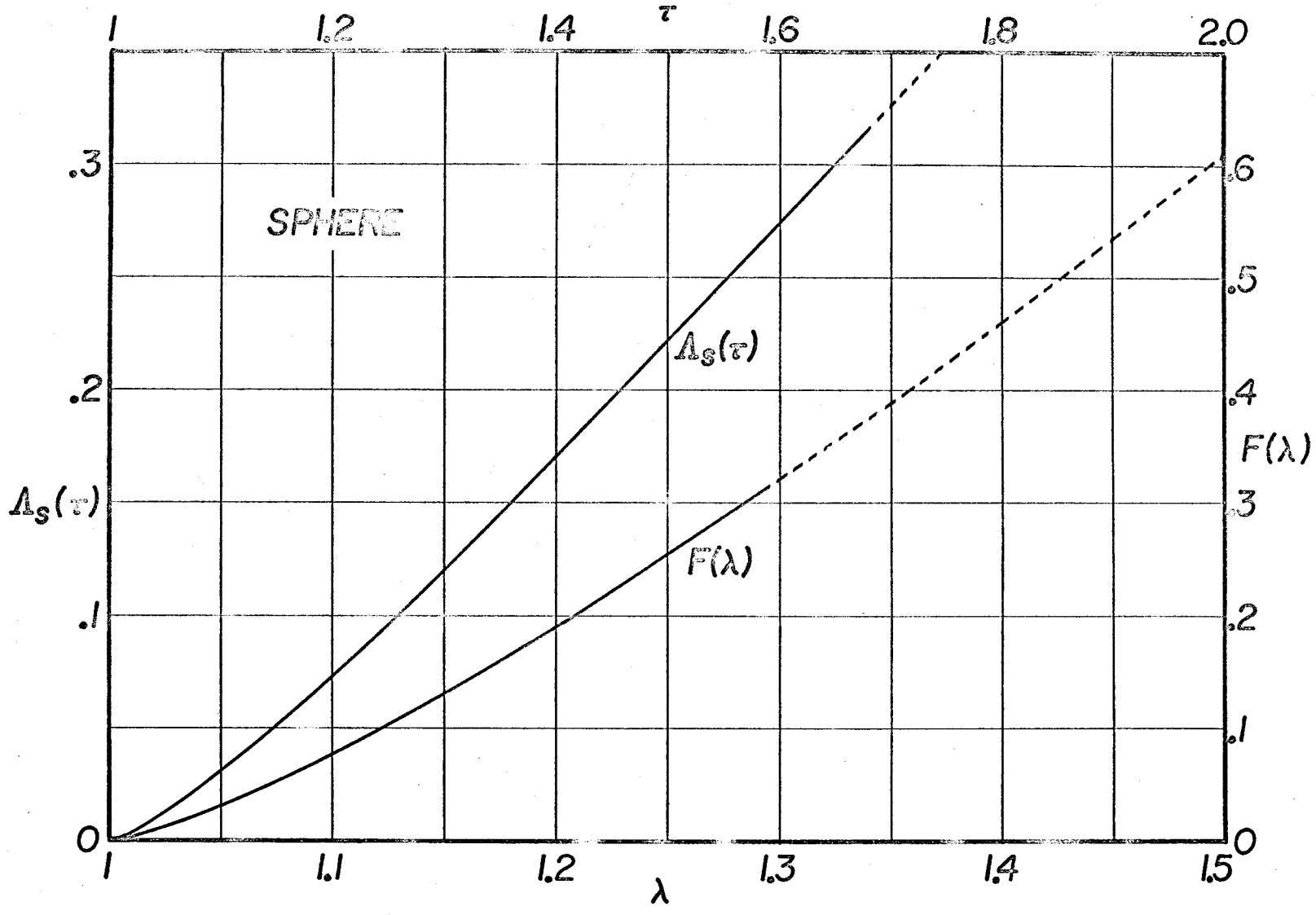

643081

Figure 22

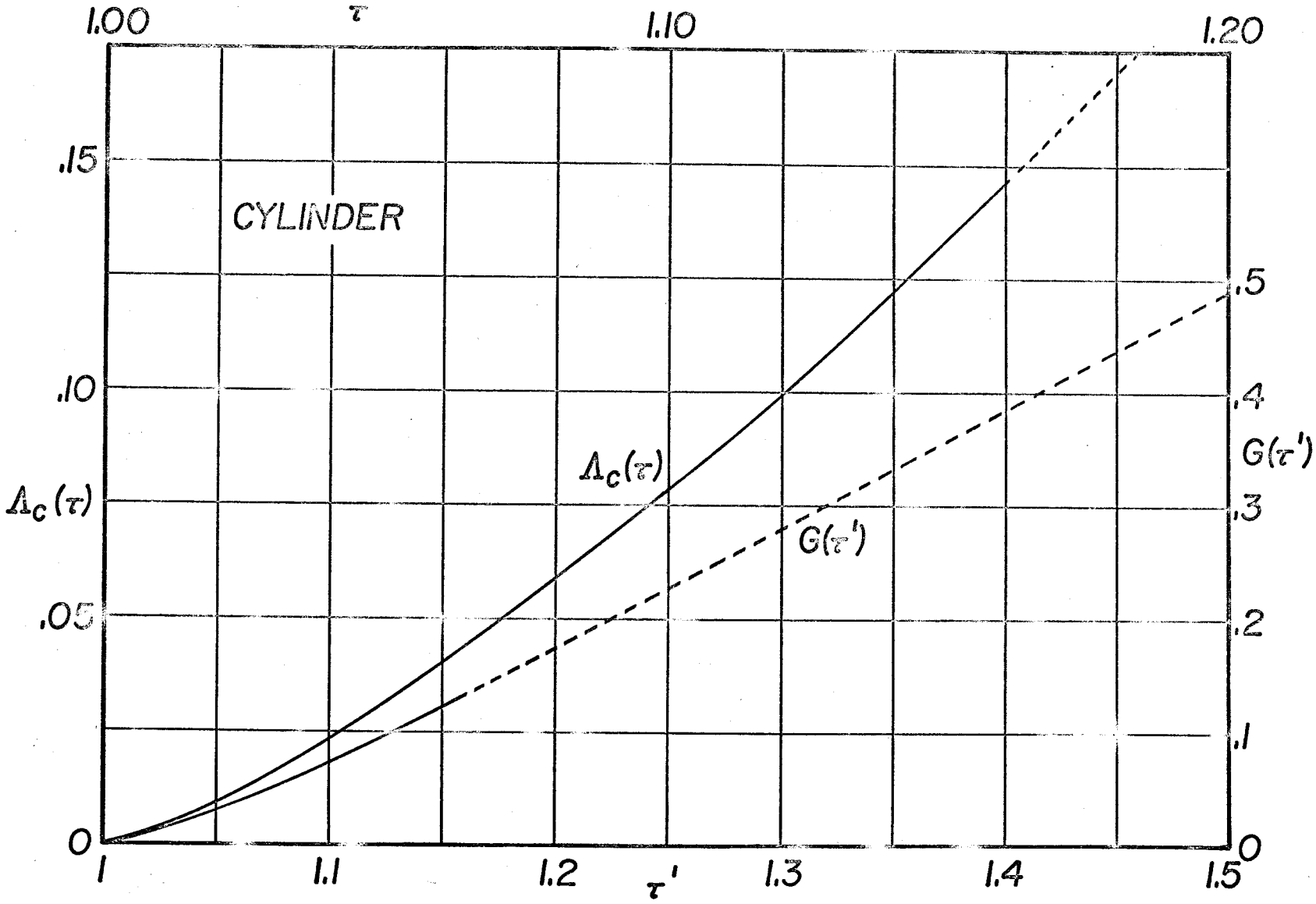

Figure 23

643078

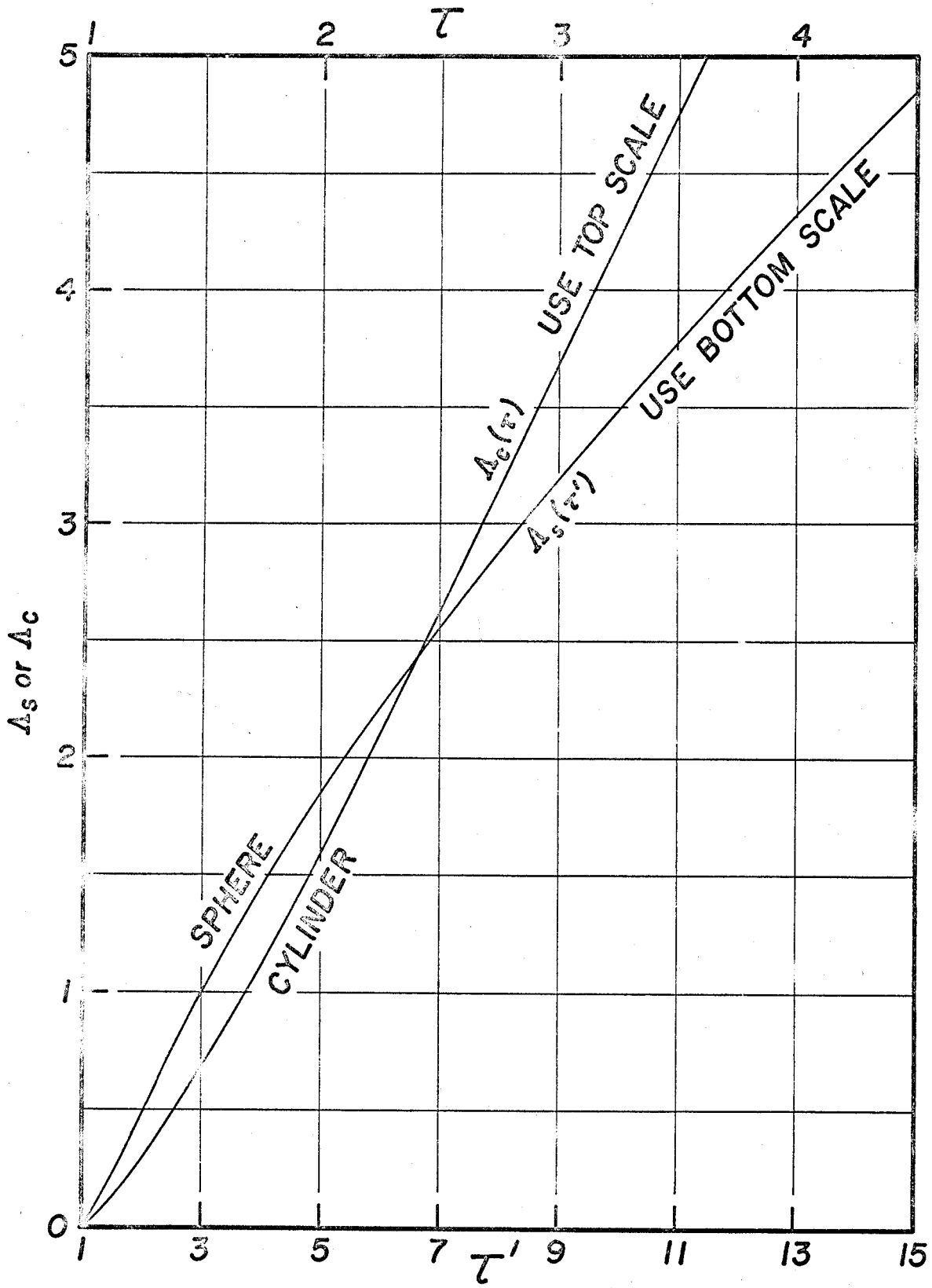
τ
1
2
3
4
5
4
3
2
1
0
Λ_s or Λ_c
$\Lambda_c(\tau)$
USE TOP SCALE
$\Lambda_s(\tau')$
USE BOTTOM SCALE
SPHERE
CYLINDER
1
3
5
7
τ'
9
11
13
15
643236

Figure 24

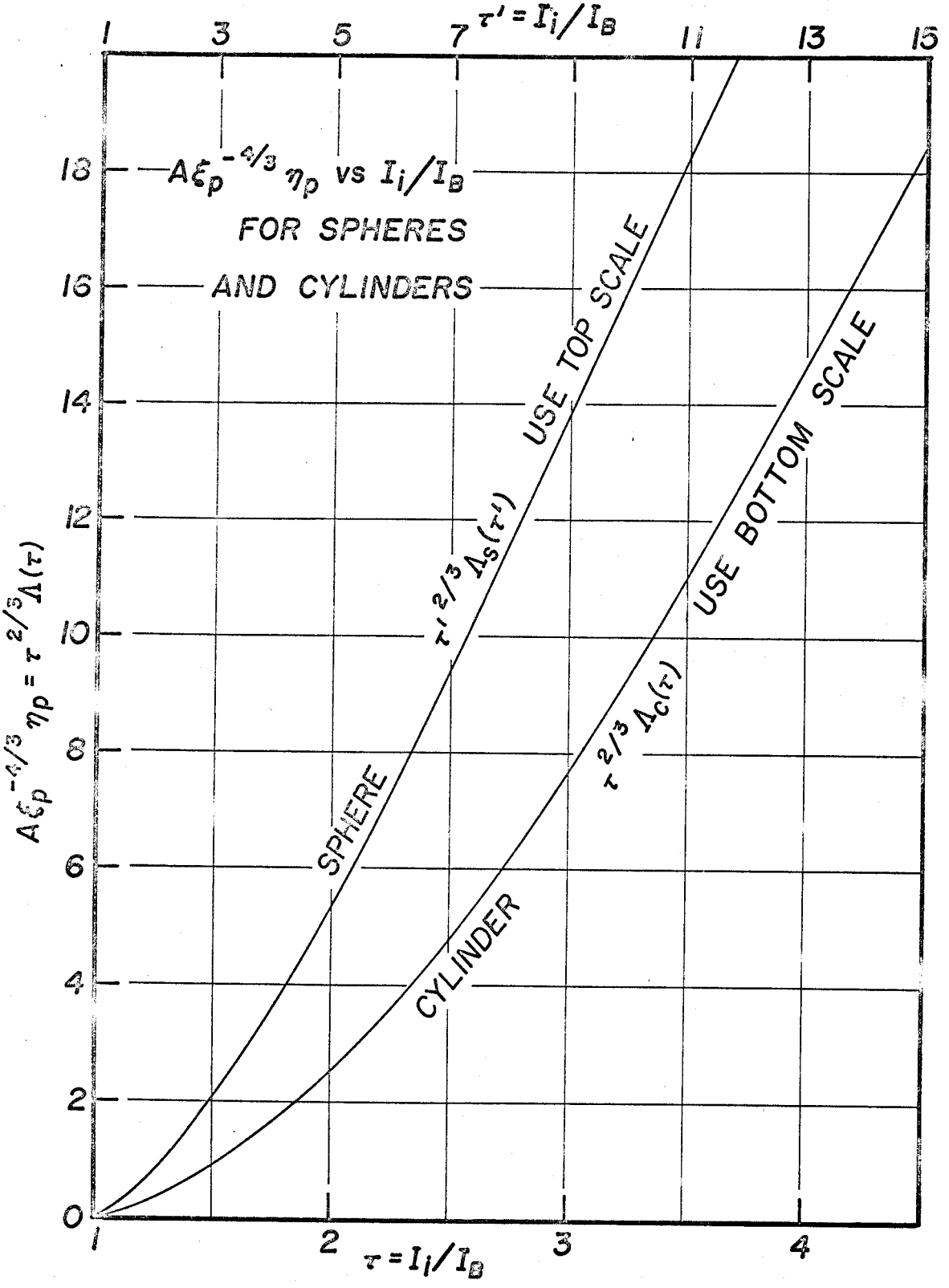
$A\xi_p^{-4/3}\eta_p$ vs I_i/I_B
FOR SPHERES
AND CYLINDERS
$\tau' = I_i/I_B$
$\tau = I_1/I_B$
$A\xi_p^{-4/3}\eta_p = \tau^{2/3}\Lambda(\tau)$
$\tau'^{2/3}\Lambda_s(\tau')$ USE TOP SCALE
$\tau^{2/3}\Lambda_c(\tau)$ USE BOTTOM SCALE
SPHERE
CYLINDER
0
2
4
6
8
10
12
14
16
18
1
3
5
7
11
13
15
1
2
3
4
643235

Figure 25

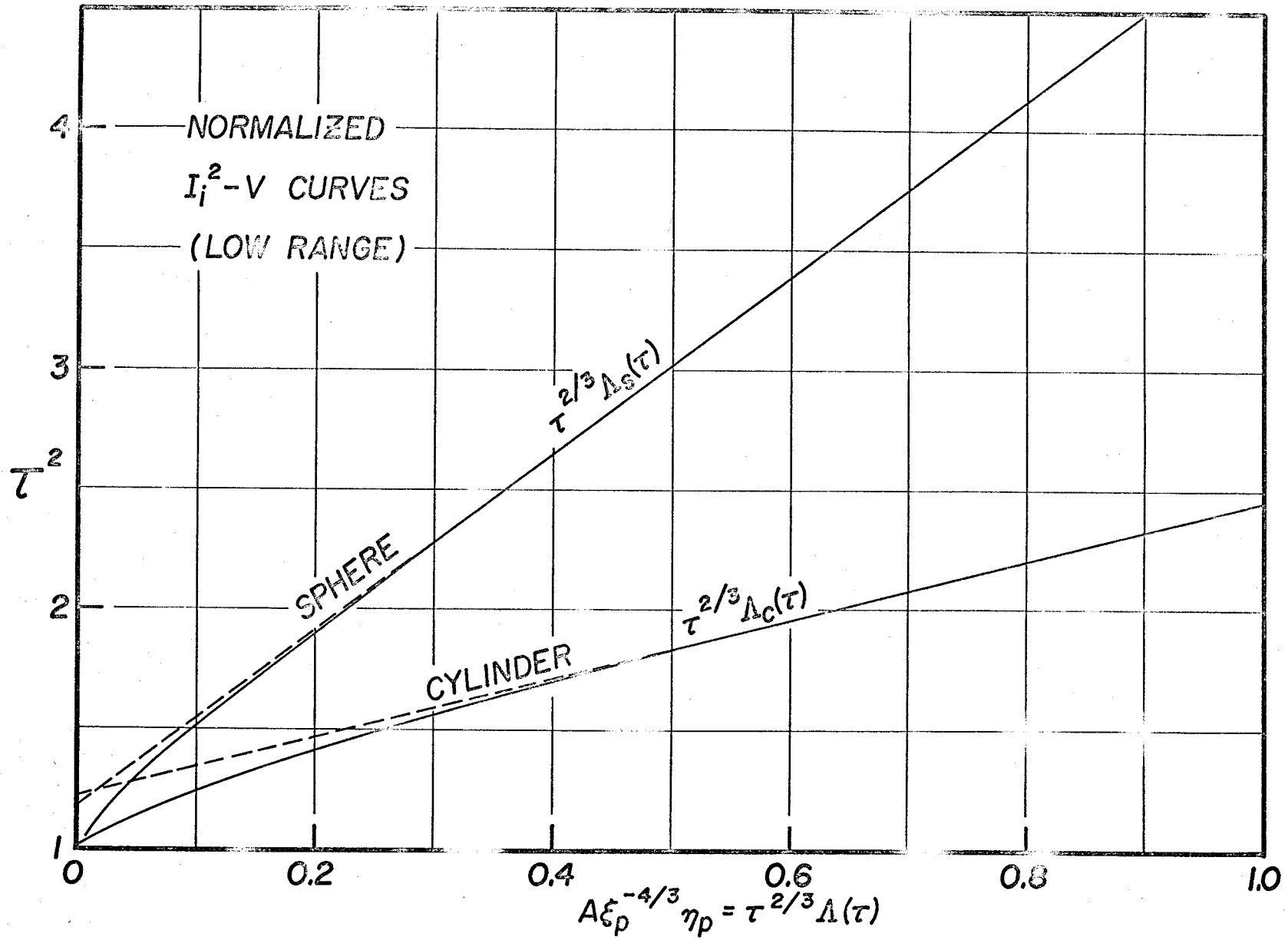

643234

Figure 26

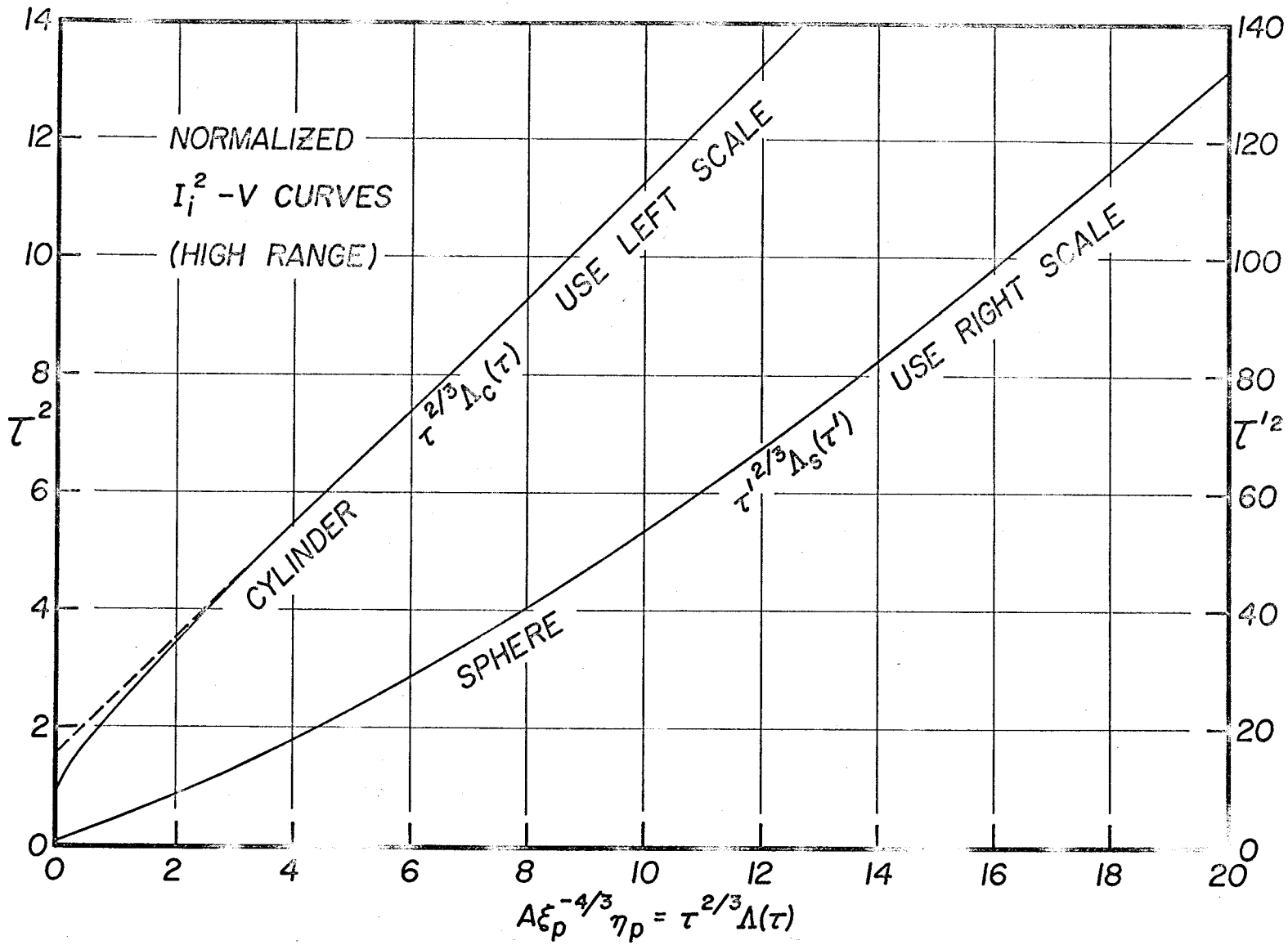

643237

Figure 27